



Characterisation of the multi-scheme chemical ionisation inlet-2 and the detection of gaseous iodine species

Xu-Cheng He^{1,2}, Jiali Shen¹, Siddharth Iyer³, Paxton Juuti⁴, Jiangyi Zhang¹, Mrisha Koirala⁵, Mikko M. Kytökari⁵, Douglas R. Worsnop^{1,6}, Matti Rissanen^{3,5}, Markku Kulmala^{1,7,8,9}, Norbert M. Maier⁵, Jyri Mikkilä⁴, Mikko Sipilä¹, and Juha Kangasluoma^{1,4}

¹Institute for Atmospheric and Earth System Research/Physics, Faculty of Science, University of Helsinki, 00014 Helsinki, Finland

²Finnish Meteorological Institute, 00560 Helsinki, Finland

³Aerosol Physics Laboratory, Faculty of Engineering and Natural Sciences, Tampere University, 33014 Tampere, Finland

⁴Karsa Ltd., 00560 Helsinki, Finland

⁵Department of Chemistry, Faculty of Science, University of Helsinki, 00014 Helsinki, Finland

⁶Aerodyne Research, Inc., Billerica, 01821 MA, USA

⁷Helsinki Institute of Physics, University of Helsinki, 00014 Helsinki, Finland

⁸Joint International Research Laboratory of Atmospheric and Earth System Sciences, School of Atmospheric Sciences, Nanjing University, 210023 Nanjing, China

⁹Aerosol and Haze Laboratory, Beijing Advanced Innovation Center for Soft Matter Science and Engineering, Beijing University of Chemical Technology, 100029 Beijing, China

Correspondence: Jiali Shen (jiali.shen@helsinki.fi) and Xu-Cheng He (xucheng.he@helsinki.fi)

Abstract. The multi-scheme chemical ionisation inlet 1 (MION1) allows fast switching between measuring atmospheric ions without chemical ionisation and neutral molecules by multiple chemical ionisation methods. In this study, the upgraded multi-scheme chemical ionisation inlet 2 (MION2) is presented. The new design features improved ion optics that increase the reagent ion concentration, a generally more robust operation and the possibility to run multiple chemical ionisation methods with the same ionisation time.

To simplify the regular calibration of MION2, we developed an open-source flow reactor chemistry model (MARFORCE) to quantify the chemical production of sulfuric acid (H_2SO_4), hypiodous acid (HOI) and hydroperoxyl radical (HO_2). MARFORCE simulates convection-diffusion-reaction processes inside typical cylindrical flow reactors with uniform inner diameters. The model also provides options to simulate the chemical processes 1) when two flow reactors with different inner diameters are connected together and 2) when two flows are merged into one (connected by a Y-shape tee), but with reduced accuracy. Additionally, the chemical mechanism files in the model are compatible with the widely-used Master Chemical Mechanism, thus allowing future adaptation to simulate other chemical processes in flow reactors.

We further carried out detailed characterisation of the bromide (Br^-) and nitrate (NO_3^-) chemical ionisation methods with different ionisation times. We calibrated H_2SO_4 , HOI and HO_2 by combining gas kinetic experiments with the MARFORCE model. Sulfur dioxide (SO_2), water (H_2O) and molecular iodine (I_2) were evaluated using dilution experiments from a gas cylinder (SO_2), dew point mirror measurements (H_2O), and a derivatization approach in combination with high-performance liquid chromatography quantification (I_2), respectively. We find that the detection limit is negatively correlated with the frag-



mentation enthalpy of the analyte-reagent ion (Br^-) cluster, i.e., a stronger binding (larger fragmentation enthalpy) leads to a lower detection limit. Additionally, a moderately longer reaction time enhances the detection sensitivity thus decreasing the detection limit. For example, the detection limit for H_2SO_4 is estimated to be 2.9×10^4 molec. cm^{-3} with a 300 ms ionisation time. A direct comparison suggests that this is even better than the widely-used Eisele-type chemical ionisation inlet.

While the NO_3^- chemical ionisation method is generally more robust, we find that the Br^- chemical ionisation method (Br^- -MION2) is significantly affected by air water content. Higher air water content results in lower sensitivity for HO_2 and SO_2 within the examined conditions. On the other hand, a steep sensitivity drop of H_2SO_4 , HOI and I_2 is only observed when the dew point is greater than 0.5-10.5 °C (equivalent to 20-40 % RH; calculated at 25 °C hereafter). Future studies utilising atmospheric pressure Br^- chemical ionisation method, including Br^- -MION2, should carefully address the humidity effect on a molecular basis. By combining methods such as water-insensitive NO_3^- -MION2 with Br^- -MION2, MION2 should be able to provide greater details of air composition than either of these methods alone.

Combining instrument voltage-scanning, chemical kinetic experiments and quantum chemical calculations, we find that the HIO_3 detection is not interfered with by iodine oxides under atmospherically relevant conditions. The IO_3^- , $\text{HIO}_3\text{NO}_3^-$ and HIO_3Br^- ions measured using the Br^- and NO_3^- chemical ionisation methods are primarily, if not exclusively, produced from gaseous HIO_3 molecules.

1 Introduction

Chemical ionisation mass spectrometer (CIMS) has been widely used in atmospheric chemistry and aerosol formation studies due to its versatility and high sensitivity in measuring trace level gaseous species (see e.g., Eisele and Tanner (1993); Munson and Field (1966); Hansel et al. (1995); Huey (2007); Kirkby et al. (2011); Ehn et al. (2014); Lee et al. (2014); Berndt et al. (2016); Sipilä et al. (2016); Laskin et al. (2018); He et al. (2021b)). With chemical ionisation methods, an analyte is charged either by 1) receiving charge (proton, electron or ion) from the reagent ion or 2) forming relatively stable cluster with the reagent ion. Mass spectrometers further measure the charged analyte-containing ions to obtain their molecular information.

Various chemicals have been used to produce reagent ions; the most commonly used reagent ions include nitrate (NO_3^- , Eisele and Tanner (1993)), acetate ($\text{C}_2\text{H}_3\text{O}_2^-$, Veres et al. (2008)), iodide (I^- , Caldwell et al. (1989)), hydronium (H_3O^+ , Lagg et al. (1994)), and sporadically also e.g., bromide (Br^- , Caldwell et al. (1989)) and ammonium (NH_4^+ , Westmore and Alauddin (1986)). These reagent ions transfer charges to or form clusters with distinct subsets of analytes of interest. The detection of an analyte-containing ion is additionally limited by its transmission through the ion optics of the mass spectrometers, since collision-induced cluster fragmentation may remove the signature of the original analyte. A strongly bonded analyte-reagent ion cluster has a substantially higher chance to reach the detector compared to weakly bonded ones (Passananti et al., 2019). Therefore, a smart selection of a chemical ionisation method that can maintain the signature of the analyte is desired. For example, the NO_3^- -CIMS has been widely used to detect sulfuric acid (H_2SO_4) (Eisele and Tanner, 1993) and highly oxygenated organic molecules (Ehn et al., 2014). I^- -CIMS is regularly used to detect semi-volatile organic compounds (Lee et al.,



2014), bromine and chlorine-containing species (Liao et al., 2014; Wang et al., 2019) and e.g., dinitrogen pentoxide (N_2O_5) (Thornton et al., 2010). $\text{C}_2\text{H}_3\text{O}_2^-$ -CIMS was used to detect small organic acids (Veres et al., 2008) and highly oxygenated organic compounds (Berndt et al., 2016). The bromide chemical ionisation method has recently been used to detect species such as HO_2 (Sanchez et al., 2016) and H_2SO_4 (Wang et al., 2021a). The detection of a series of halogenated species by the
55 Br^- chemical ionisation method was first demonstrated by He (2017). Detailed characterisation of the Br^- chemical ionisation method utilising the multi-scheme chemical ionisation inlet 1 (MION1) was presented in several of our earlier studies (Wang et al., 2021a; Tham et al., 2021; He et al., 2021b). Multiple species were successfully calibrated using either analytical methods or inter-instrument comparison, including H_2SO_4 , I_2 , Cl_2 and HOI (Tham et al., 2021; Wang et al., 2021a). Among the calibrated species, H_2SO_4 and I_2 were shown to be detected at the collision limit (highest sensitivity).

60

Ideally, all of the mentioned analytes can be measured simultaneously by utilising all of the corresponding CIMS methods at the same time in ambient observations or in complex laboratory experiments. However, CIMS instruments are expensive and research institutes are regularly limited by available instrumentation. An alternative approach is using chemical ionisation inlets capable of switching reagent ions. Many switchable systems have been developed previously, such as for proton transfer
65 reaction mass spectrometers (Jordan et al., 2009; Breitenlechner et al., 2017; Pan et al., 2017) and other chemical ionisation mass spectrometers (Hearn and Smith, 2004; Smith and Španěl, 2005; Agarwal et al., 2014; Brophy and Farmer, 2015). A common feature of these techniques is using a reduced-pressure ion-molecule reaction chamber, thus unavoidably diluting the gas molecules of interest by orders of magnitude. While the detection limit of an instrument is also affected by other factors, it is commonly observed that chemical ionisation inlets operating at reduced pressures have higher limits of detection compared
70 to atmospheric pressure chemical ionisation inlets. For instance, reduced pressure inlets reported detection limits of various organic compounds from sub-pptv (parts per trillion by volume) to hundreds of pptv levels (Lee et al., 2014; Brophy and Farmer, 2015), while the best-performing atmospheric pressure chemical ionisation inlets regularly detect vapours at ppqv (parts per quadrillion by volume) levels for selected acids and highly oxygenated organic vapours using the same time-of-flight mass spectrometer (Jokinen et al., 2012; Ehn et al., 2014; He et al., 2021b).

75

To lower the limit of detection of switchable reagent ion chemical ionisation systems, we developed the MION1 inlet for fast switching of reagent ion chemistry operating at atmospheric pressure (Rissanen et al., 2019). This technique has mostly been deployed to detect sulfuric acid and halogenated species using either NO_3^- or Br^- chemical ionisation methods (Rissanen et al., 2019; Tham et al., 2021; He et al., 2021b; Wang et al., 2021a; Finkenzeller et al., 2022).

80

However, the remaining problems of the MION1 include 1) the limit of detection of the MION1 is lower compared to another widely used atmospheric pressure chemical ionisation inlet (noted as "Eisele inlet" hereafter) (Eisele and Tanner, 1993; Jokinen et al., 2012; Wang et al., 2021a) and 2) the ion-molecule reaction times for different chemical ionisation methods had to be different, owing to the design that the chemical ionisation units are aligned and attached on a cylindrical tube at vary-
85 ing distances. These problems could limit its applicability to the detection of vapours at extremely low concentrations (e.g., at



10^5 to 10^6 molec. cm^{-3} or 5 to 50 ppqv) and the interpretation of the species detected by different chemical ionisation methods.

In this study, we present an upgraded MION inlet (noted as "MION2" hereafter) which addresses these problems. Laboratory experiments were carried out to characterise this inlet using analytical methods and a newly-developed open-source kinetic model. As halogen anion-based chemical ionisation methods (e.g., I^-) are commonly affected by air water content (Kercher et al., 2009; Mielke et al., 2011; Woodward-Massey et al., 2014; Lee et al., 2014), we additionally performed systematic examinations of the impact of air water content on the detection of Br^- -MION2.

2 Methods

2.1 Characterisation of the MION2 inlet

The ionisation inlet used in this paper is the upgraded multi-scheme chemical ionisation inlet, MION2 (Karsa Ltd.). The inlet is designed to be capable of measuring neutral molecules using chemical ionisation methods and detecting atmospheric ions by disabling chemical ionisation. It allows fast switching between two or more (up to six) chemical ionisation methods to selectively measure gaseous species at ambient pressure. The inlet accommodates three bipolar ion sources per reaction time, which is defined by the sample flow rate and the distance from the ion injection port to the instrument pinhole (Figure 1). For the longer reaction time, the length of the connecting pipe between the sources can be adjusted, i.e., the ionisation time can be modified. Therefore, the new design of MION2 allows it to operate two chemical ionisation methods with the same ionisation time to allow a direct comparison which was not possible with the MION1. In this study, we deployed the inlet with two chemical ionisation methods (NO_3^- and Br^-) and two reaction times to understand the inlet characteristics. To clarify the different positions of the ionisation inlet, we refer to the ion source 3 cm away from the mass spectrometer as tower 1 (T1), and the source 25 cm away from the mass spectrometer as tower 2 (T2) throughout the paper (Figure 1).

Supplementary Figure A1 presents the conceptual schematic for one of the ion sources with airflow and ion paths. The whole source is attached to an electrically grounded 24 mm inner diameter tube with 22.5 standard litres per minute (slpm) sample flow, where the target molecules are charged by reacting with the reagent ions (NO_3^- or Br^-). In this case, the reaction time of the targeted molecules and charged reagent ions for tower 1 was ca. 35 ms, and for tower 2, 300 ms. A neutral reagent inflow is a stream of nitrogen or air enriched with reagent vapour (CH_2Br_2 or HNO_3 in this paper), which is then fed into the ion source and ionised by a soft x-ray (Hamamatsu L12535, 4.9 keV). The charged reagent ions are then guided by an electric field into the sample flow. The electric field inside the ion source is created with concentric stainless steel electrode plates with different size orifices (diameters between 5-10 mm), added resistances between every two plates, and two high voltages (ca. 2500 V and 250 V). The lower of these two voltages determines if the reagent ions pass through the last orifice in the deflector electrode into the sample flow, effectively turning the ionisation on and off, and enabling the fast switching between ion sources.



Compared with the MION1 (Rissanen et al., 2019), where the source reagent flow was defined by the neutral reagent inflow and the outflow (i.e., exhaust), MION2 has an additional purge flow to prevent the sample flow from entering the ion source. The purge flow consists of the same nitrogen, or synthetic air, that is used to create the reagent flow. The purge flow splits in two upon entering the ion source: one preventing the sample from entering and the other keeping the neutral reagent from entering the sample flow. With the MION1, one had to choose between possibly contaminating the sample pipe with the neutral reagent, or pulling sample air into the ion source potentially contaminating the ion source, e.g., it sometimes results in salt formation in the ion source or potentially results in uncontrolled ion chemistry within the inlet leading to detection biases. Operational testing in ambient measurements indeed showed that MION2 is significantly more stable than MION1. The ion optics inside the ion sources in MION2 have been upgraded which increase the reagent ion transmission compared to the MION1 by about an order of magnitude.

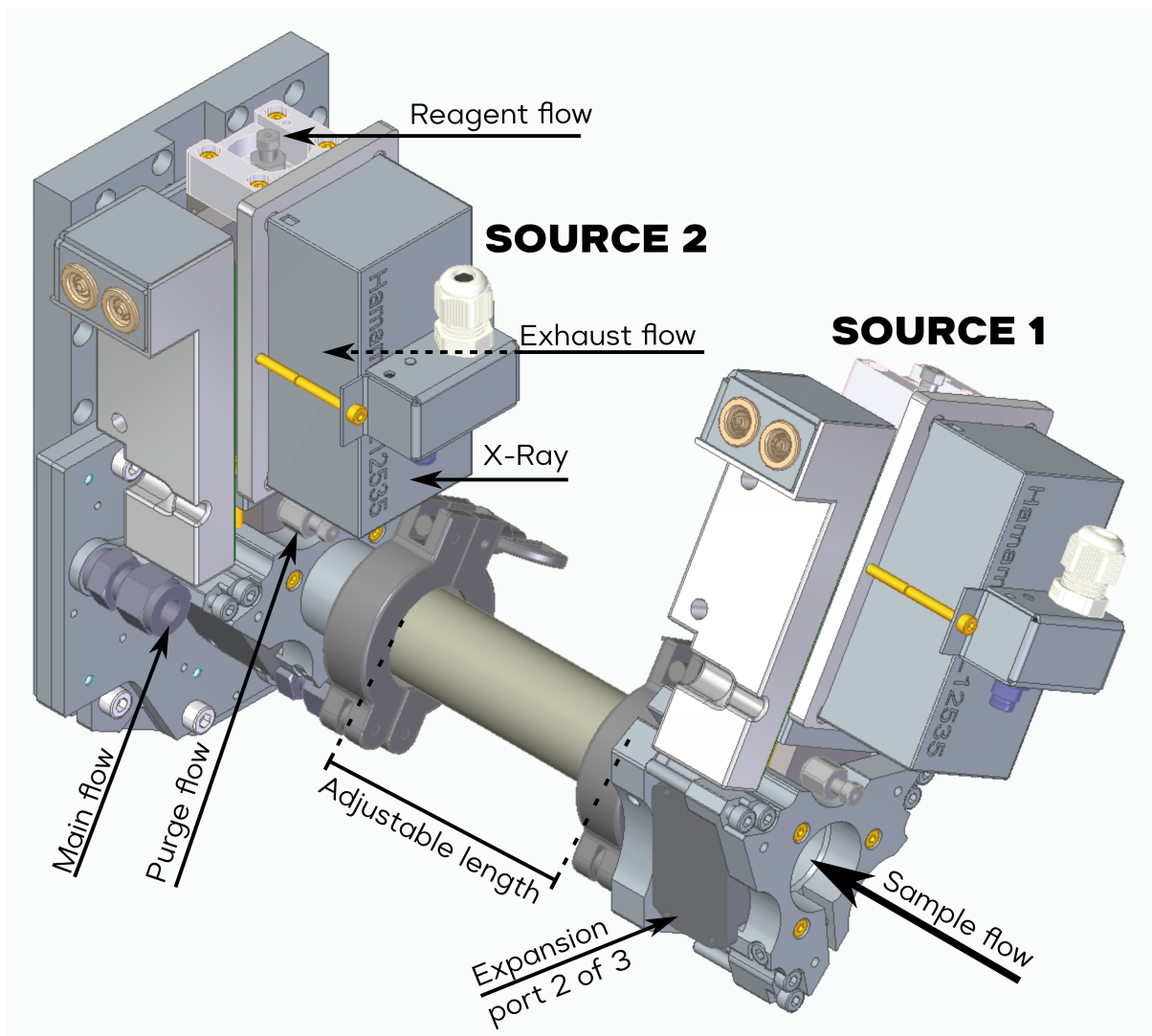


Figure 1. Schematic of the MION2 inlet illustrating its gas flows and ion paths. The new design increases the primary ion concentration and allows the operation of multiple chemical ionisation methods with the same ionisation time.

2.2 Experimental setup

2.2.1 Calibration of inorganic species

130 In order to characterise the MION2 inlet, we utilised an experimental setup as shown in Figure A2, which comprises three sections: the flow reactor section, the chemical ionisation inlet (MION2) section, and an Atmospheric Pressure interface Time-of-Flight mass spectrometer (APi-TOF, Aerodyne Inc., Junninen et al. (2010)). The flow reactor section consists of a calibration source and various gas feeds. Synthetic air (Woikoski OY, Finland; purity $\geq 99.999\%$ with 20.9% O_2), nitrogen (N_2 , Woikoski



OY, Finland; purity $\geq 99.999\%$), and sulfur dioxide (SO_2 , Air Products, USA; 99.5 % purity) were injected by mass flow controllers (MFCs) connected to standard gas cylinders or tanks and they were pre-mixed before the calibration source. Molecular iodine (I_2) was produced either from a homemade permeation tube or a commercial permeation tube (VICI Metronics) by blowing a stream of nitrogen (50 millilitres-per-minute, mlpm) at controlled temperatures (120 to 140 °C). The temperature of the permeation tubes was controlled by an electronically controlled heating mantle to enable adjustable yet stable iodine concentrations. H_2O was controlled by an adjustable stream of nitrogen passing through a water bubbler.

140

The calibration source was mainly used to calibrate H_2SO_4 , HO_2 and HOI. The H_2SO_4 calibration has been detailed in Kürten et al. (2012) and the HOI calibration has been presented in Tham et al. (2021) and Wang et al. (2021a). Briefly, a known amount of OH radical is produced by a mercury lamp (UVP Pen-Ray) in the calibration source which further reacts with an excess amount of SO_2 or a moderate amount of I_2 to produce either H_2SO_4 or HOI as the final products. As the HO_2 radical is a by-product of the H_2SO_4 calibration, HO_2 calibration was simultaneously carried out at the H_2SO_4 calibration. The measured concentrations of H_2SO_4 , HOI and HO_2 were predicted using a numerical model adopting two-dimensional convection-diffusion-reaction equations. As the numerical model needed to do the calibration is not yet available to the public, this study further develops an open-source Python library for such tasks (Shen and He, 2023).

145

The SO_2 calibration is relatively straightforward and the calibrator source is not needed. The SO_2 flow from the SO_2 gas cylinder was diluted with humidified nitrogen and the mixed sample was fed into the inlet. The measured $\text{SO}_2 \cdot \text{Br}^-$ signal is further compared with the estimated SO_2 concentration to derive a calibration factor.

150

Absolute H_2O concentration was calibrated using a dew point mirror (DewMaster Chilled Mirror Hygrometer, EdgeTec). The dew point mirror drew and measured a branch of the humidified flow before it entered the MION2 inlet tube.

155

2.2.2 Calibration of molecular iodine

Although Br^- chemical ionisation method has been shown to be extremely sensitive in the molecular iodine (I_2) detection (He, 2017; Wang et al., 2021a; Tham et al., 2021), the quantification of the measured $\text{I}_2 \cdot \text{Br}^-$ signal remains challenging. This is primarily contributed by two factors: 1) the current Br^- -MION1/2 have a detection upper limit of a few hundred pptv of I_2 , beyond which the reagent ions get depleted and the measurement is non-linear, 2) on the contrary, spectroscopic and other methods could be limited by their high detection limits and may not be able to detect I_2 at appropriate levels. Therefore, the key is to find sensitive methods to quantify gaseous I_2 at tens to hundreds of pptv levels.

160

We have previously calibrated the I_2 measurement of Br^- -MION1 using a cavity-enhanced differential optical absorption spectroscopy (CE-DOAS) instrument (Wang et al., 2021a), an UV/Vis spectrophotometer and an inductively coupled plasma mass spectrometer (ICP-MS) (Tham et al., 2021; Wang et al., 2021a). As none of these instruments is available for this study,

165



we further adapted an alternative method.

170 The collection of the I₂ sample followed exactly the same procedure as described in our previous studies (Tham et al., 2021;
Wang et al., 2021a). Briefly, 50 standard cubic centimetres per minute (sccm) nitrogen carrier gas flow was passed through an
I₂ permeation tube for 300 min, under 120-140 °C. The nitrogen carrier stream containing the released I₂ was bubbled through
an Schlenk-type impinger charged with 20 mL of hexane kept at -70 °C by a dry ice/acetone bath. After completion of the
sampling process, the absorption flasks were allowed to warm to the ambient temperature and sealed with a Teflon-coated glass
stopper. The solution was stored at 4 °C until further processing.

175

Inspired by Mishra et al. (2000), I₂ was converted into an essentially non-volatile and stable derivative, followed by quanti-
fication of the latter using gas or liquid chromatography. Mishra et al. (2000) quantified I₂ in aqueous matrices by GC/MS after
I₂ reacting with 2,6-dimethylaniline to form the corresponding 4-iodo-derivative. An adaptation of this method was required
as the iodine to be determined was diluted in hexane. Specifically, the iodine derivatisation reaction was conducted directly
180 with the hexane solutions in presence of an aqueous buffer, to reduce losses associated with a hexane-to-water transfer. To
avoid any losses of the volatile I₂ through evaporation, the reaction was conducted in hermetically sealed headspace vials,
with efficient phase mass transfer being facilitated by vigorous magnetic stirring. Control of the pH of the buffer was crucial
for achieving high derivatisation yields, with pH at 7.00 providing the most favourable level of conversion after 2 hours. At-
tempts to perform the derivatisation reaction under homogeneous conditions in hexane in the presence of a variety of soluble
185 organic bases (e.g., tertiary amines) returned poor yields and led to the formation of several side products, most probably due
to iodine oxidation. Experiments using 1.00 mL aliquots of the I₂ sample solutions under investigation produced the derivative
at the limit of detection, precluding a reliable quantification of the derivative by the reverse phase high-performance liquid
chromatography (RP-HPLC/UV). To improve the analytical sensitivity, 10 mL aliquots of the iodine sample solution were
employed for derivatisation. To boost the sensitivity further, a high volume (15 μL) of the concentrated derivatisation solution
190 was injected into the HPLC system. Unfortunately, the hexane in the injection solution and the high injection volume gave rise
to retention time instability and peak distortion. Subsequent optimisation of the chromatographic method provided robust re-
verse phase chromatographic conditions. Specifically, this was achieved by using relatively weakly eluting isocratic conditions
for sample elution, followed by strongly eluting conditions for column cleaning and reconditioning. Using the fully optimised
protocol, the derivative could be readily quantified for 0.17 to 11.05 μg mL⁻¹ initial iodine concentrations, with the LOD and
195 LOQ (limit of quantification) being 0.012 μg mL⁻¹ and 0.035 μg mL⁻¹. Using this method, the hexane solution obtained
by absorption of iodine from the permeation tube was found to contain 0.26 μg iodine mL⁻¹. Considering a total sample vol-
ume of 20 mL, the iodine output rate of the permeation tube under the employed conditions was calculated to be 17.3 ng min⁻¹.

It is worth noting that the sensitivity of the current method can be further improved by employing more sensitive separation
200 and/or detection techniques, e.g., LC/MS or GC/MS.



2.2.3 Humidity dependence of analyte detection

An important part of the characterisation is examining the impact of water on the detection of MION2 when utilising the bromide chemical ionisation method. Since H₂O is needed in the calibration source to produce OH radicals which in turn produce either H₂SO₄ or HOI, we additionally added a dilution flow which joins after the calibration source using a Y piece (see Figure A3). This experimental design enables changing the sample absolute humidity independent of the OH production rate in the calibration source. During the experiments with varying humidity, the total flows of the dilution part and the flow reactor section were kept constant, while the relative humidity of the dilution flow was varied by mixing different combinations of dry and humidified flows. In this way, we were able to keep the systematic errors, resulting from the mixing of the dilution and sample flows, constant. By comparing the relative signal intensities of analyte-containing ions, we could examine the influence of water on the detection of different analytes (e.g., H₂SO₄, HOI and HO₂).

2.2.4 Quartz flow reactor setup

In order to study the sensitivity of Br⁻-MION2 to other oxidised iodine species, e.g., IO, OIO, HIO₃, I₂O₃, I₂O₄ and HIO₂, a quartz flow reactor with an outer diameter of 2.54 cm and a length of 94 cm was used. A green LED was hung on top and in parallel to the quartz flow reactor to initiate iodine photo-chemistry. In order to keep the temperature and light uniformity in the quartz flow reactor, the flow reactor was wrapped together with the green LED light by aluminium foil. The schematics of the setup are shown in supplementary Figure A4.

2.3 MARFORCE model description

As described above, calibration of H₂SO₄, HO₂, and HOI requires a numerical model to simulate the chemical dynamics in the calibration source and inlet tube. This process can be simplified into a two-dimensional convection-diffusion-reaction problem. The concept of such a model was illustrated elsewhere (Kürten et al., 2012), specifically for the calibration of H₂SO₄. Our earlier studies also presented a numerical model for HOI calibration with similar principles but a simplified iodine chemistry scheme was instead implemented (Tham et al., 2021; Wang et al., 2021a). However, neither of these studies made the calibration scripts openly available and the scripts are not flexible in adopting different chemistry schemes. Therefore, we developed an open-source two-dimensional flow reactor model (MARFORCE, Marine Atmospheric paRticle FORMation and ChEmistry) for these tasks. MARFORCE was built in Python and is hosted in GitHub (Shen and He, 2023). Thus it can be freely accessed. The model has two major components: 1) the fluid dynamics simulation module and 2) the gas-phase photo-chemistry module.

2.3.1 Convection-diffusion-reaction equation

The MARFORCE model utilises a two-dimensional convection-diffusion-reaction equation to simulate the fluid dynamics, photo-chemistry and chemical reactions in a cylindrical flow reactor. The convection-diffusion-reaction equation has been derived and discussed extensively in the literature (Gormley and Kennedy, 1948; Kürten et al., 2012) and is only briefly



discussed here:

$$\frac{\partial c_i}{\partial t} = D_i \left(\frac{1}{r} \frac{\partial c_i}{\partial r} + \frac{\partial^2 c_i}{\partial r^2} + \frac{\partial^2 c_i}{\partial z^2} \right) - \frac{2Q}{\pi R^2} \left(1 - \frac{r^2}{R^2} \right) \frac{\partial c_i}{\partial z} + P \quad (1)$$

where i corresponds to a specific chemical (e.g., H_2SO_4), the c_i is the concentration, D_i is the diffusion coefficient, r is the distance in the radial direction, R is the radius of the flow reactor, z is the distance in the axial direction and P shows the production (positive values) or loss (negative values) rate due to chemical reactions. As the flow in tangential direction is symmetrical, the $\frac{1}{r^2} \frac{\partial^2 c_i}{\partial \theta^2}$ term has been ignored.

The diffusion coefficient in the model can be defined in two ways: 1) manually defined using experimental values or calculated by kinetic theory or 2) calculated based on elemental composition using Fuller's method (Fuller et al., 1966).

240

The convection and diffusion processes were validated against a theoretical prediction by Alonso et al. (2016). A fixed amount of H_2SO_4 was set at the first cross-section of the MARFORCE simulation and H_2SO_4 was further carried to the outlet of a cylinder only by convection and diffusion processes. Comparing the H_2SO_4 profiles at the outlet yields on average a 0.4 % difference between the MARFORCE model and the theoretical prediction by Alonso et al. (2016) (supplementary Figure A5). This suggests that the convection and diffusion processes in the MARFORCE model are well simulated.

245

2.3.2 Gas-phase photo-chemistry

The photolysis and chemical reactions in the H_2SO_4 , HO_2 and HOI calibrations can be simulated by a set of differential equations which describe the production and loss of various species. To make the MARFORCE model more versatile, the model was designed to accommodate the input file format from the Master Chemical Mechanism (MCM) (Jenkin et al., 1997; Saunders et al., 2003), a near-explicit chemistry mechanism for numerous organic precursors. The scripts used to compile and interpret MCM mechanisms were adapted from O'Meara et al. (2021). The input file extracted from MCM is reshaped and the reaction equations, reaction rate coefficients, reactants, products, their indices, and stoichiometric numbers are generated accordingly. The temperature and pressure dependence of reaction rate coefficients are taken into consideration. Finally, differential equations for each species based on its production and loss processes are produced and solved. Additionally, the MARFORCE model leaves an option to set abundant species as constants, so their concentrations are assumed uniform and homogeneous in the flow reactor. These species include, for example, (O_2), N_2 , SO_2 , I_2 , and H_2O in the H_2SO_4 and HOI calibration experiments. With its flexibility, the MARFORCE model can be readily adapted to simulate organic oxidation or any other experiments using a laminar flow reactor.

260

There are two default chemistry schemes provided in the MARFORCE model and they are used for the H_2SO_4 calibration and the HOI calibration, respectively. The reaction rate coefficients utilised in these two schemes are tabulated in supplementary Table A1. The most important procedure of these calibration experiments is to calculate the OH concentration. The OH concentration is determined by the photon intensity produced by the calibration source (It-product, amount of photons per cm^2



cross-section) and the absolute water content in the air passing through the calibration source. The details of the It product
265 determination can be found in Kürten et al. (2012). Briefly, the chemical actinometry method utilising the conversion of N₂O
to NO_x (primarily NO) is carried out to determine the light intensity. As the NO is less reactive compared with OH and it can
easily be measured with commercial NO_x monitors, the It-product can therefore be derived. The OH initial concentration is
further defined as

$$[\text{OH}] = It \times \sigma_{\text{H}_2\text{O}} \times \Phi_{\text{H}_2\text{O}} \times [\text{H}_2\text{O}] \quad (2)$$

270 where $\sigma_{\text{H}_2\text{O}}$ is the absorption cross-section of water vapour, $7.22 \times 10^{-22} \text{ cm}^2$ (Creasey et al., 2000), and $\Phi_{\text{H}_2\text{O}}$ is the quantum
yield (unity in this case).

2.3.3 Flow mixture

On top of the regular simulation of a cylindrical flow reactor with uniform size, the MARFORCE model also has limited skills
in 1) simulating connected two flow reactors with different sizes and 2) simulating reactions when a dilution flow is merged
275 with the sample flow through a Y-shape tee.

The first design aims to cope with the different sizes of the chemical ionisation inlet and the calibration source itself. For
example, the MION2 inlet utilises a KF25 connector with an inner diameter of 24 mm while the calibrator utilises a 3/4" tube
with an inner diameter of 15.6 mm. Our model considers an instantaneous transition between the tubes of different sizes, i.e.,
280 the chemical distributions at the last grid of the first cylinder are copied into the first grid of the second cylinder while the axial
flow speed is adjusted to the cross-section of the second cylinder. As this simplification ignores the convective transport of
species to the walls at the transition region, it likely gives the concentration upper limit at the pinhole of the mass spectrometer.
Since the inner diameter difference between the calibration source and the MION2 inlet is relatively small in this study, we
expect that the resulting uncertainty is well within the overall systematic uncertainty of -50/+100 %.

285

The second design considers that an additional dilution flow is utilised to reduce the sample water content when entering
the Br⁻-MION2 inlet. Similarly, we assume an instantaneous transition at the spot where the dilution flow is added. In this
case, both the chemical distribution and axial flow speed are changed since a new branch of flow is added. The simulation is
carried out with a two-process procedure: before and after the dilution. First, we carry out a standard simulation before adding
290 the dilution flow. Once the flow is fully developed and the chemical distribution reaches a steady state in the simulation, the
last cross-section at the grid right before adding the dilution flow is stored and recalculated into the first cross-section of the
next simulation. The second simulation is further carried out after considering the dilution flow, together with the changes in
chemical distribution and axial flow speed.

295 It should be noted that the fluid dynamics processes are overly simplified in the second design and therefore, this option
should be used with caution. In this study, this option is necessary only because investigating the detection humidity effect of



e.g., H_2SO_4 , HO_2 and HOI requires adding a dilution flow after the calibration source. In order to estimate the magnitude of error caused by the simplification of fluid dynamics, we carried out experiments comparing calibration results obtained with the first design (straight tube) and the second design (Y piece) and the results are shown in supplementary Figure A7. We find that the second design additionally introduces a 12 % higher calibration factor in the H_2SO_4 calibration and a 27 % higher calibration factor in the HOI calibration, compared with the calibrations using the first design. Therefore, the application of the second design for the purpose of this study is reasonable and does not introduce an excess amount of uncertainties. This mainly concerns the H_2SO_4 , HO_2 and HOI calibration experiments.

2.4 Quantum chemical calculations

Cluster fragmentation enthalpies were calculated using quantum chemical methods. The initial conformational sampling was performed using the Spartan '18 program. The cluster geometry was then optimized using density function theory (DFT) methods at the $\omega\text{B97X-D/aug-cc-pVTZ-PP}$ level of theory (Chai and Head-Gordon, 2008; Kendall et al., 1992). Iodine and bromine pseudopotential definitions were taken from the Environmental Molecular Sciences Laboratory (EMSL) basis set library (Feller, 1996; Peterson et al., 2003). Calculations were carried out using the Gaussian 16 program (Frisch et al., 2016). An additional coupled-cluster single-point energy correction at the $\text{DLPNO-CCSD(T)/def2-QZVPP}$ (Riplinger and Neese, 2013; Riplinger et al., 2013; Weigend and Ahlrichs, 2005) level of theory was carried out on the lowest energy conformers to refine the DFT calculated enthalpies. The coupled-cluster calculation was performed using the ORCA program version 4.2.1 (Neese, 2012).

The master equation solver for multi-energy well reactions (MESMER) program was used to investigate the ionisation chemistry of $\text{I}_2\text{O}_3 \cdot \text{HNO}_3\text{NO}_3^-$. For the $\text{I}_2\text{O}_3 \cdot \text{HNO}_3\text{NO}_3^-$ complex, Lennard-Jones potentials of $\sigma = 6.5 \text{ \AA}$ and $\epsilon = 300 \text{ K}$ were used, which are identical to those used previously for similar iodine systems (Gálvez et al., 2013). The MesmerILT method was used with a pre-exponential value of $1.26 \times 10^{-9} \text{ cm}^3 \text{ molec}^{-1} \text{ s}^{-1}$, which is equal to the $\text{I}_2\text{O}_3 + \text{HNO}_3\text{NO}_3^-$ collision rate calculated using the average dipole orientation (ADO) method. The method is described in detail by He et al. (2021a). Varying the collision rate by a factor of 3 has no effect on the MESMER results, indicating that the reported final fragmentation rate coefficients of $\text{I}_2\text{O}_3 \cdot \text{HNO}_3\text{NO}_3^-$ are not sensitive to the accuracy of the computed collision rate.

3 Results

3.1 Calibration of H_2SO_4 , HOI and HO_2 using MARFORCE

Gaseous H_2SO_4 concentration is regularly measured around the globe using the nitrate chemical ionisation method. In this study, a direct H_2SO_4 calibration has been carried out for the MION2 inlet at tower 1 using either Br^- (Br^- -MION2-T1) or NO_3^- (NO_3^- -MION2-T1) chemical ionisation methods, and additionally at tower 2 with Br^- (Br^- -MION2-T2) chemical ionisation method. The MARFORCE model is utilised to simulate the evolution of various species at the cross-section of the inlet



tube as shown in Figure 2. The predicted H₂SO₄ concentrations are further compared with the measured normalised ratios to derive calibrator factors (Table 1).

330

Table 1. Calibration coefficients and detection limits for selected species measured by the MION2 inlet and Eisele-type inlet. It should be noted that these numbers are specific to the experimental conditions and instrument tuning in our experiments. Different instrument tuning can also result in different calibration coefficients. Undesired impurities may result in elevated detection limits despite the calibration coefficients being the same for the analytes. Therefore, these numbers should not be applied to another study without carrying out the calibration experiments described in this study.

Species	Calibration coefficients (MION2 with APi1)			Detection limit			
	Tower 1 (Reaction Time = 35 ms)		Tower 2 (300 ms)	MION2		Eisele inlet	
	NO ₃ ⁻	Br ⁻	Br ⁻	Tower 1 APi2 (RH < 0.1%)	Tower 2 APi1 (RH = 3.7%)	Tower 2 APi1 (RH < 0.1%)	(160 ms) APi1 (RH = 5.6%)
H ₂ SO ₄	1.3 × 10 ¹⁰	8.1 × 10 ⁹ (RH = 0.2-23.3%)	9.8 × 10 ⁸ (RH = 0.3-11.6%)	^a 8.5 × 10 ⁴	^e 1.0 × 10 ⁵	ⁱ 2.9 × 10 ⁴	^l 7.6 × 10 ⁴
HOI	n/a	1.8 × 10 ¹⁰ (RH = 3-17%)	5.1 × 10 ⁹ (RH = 3-17%)	^a 2.2 × 10 ⁵	^f 5.9 × 10 ⁵	^j 1.6 × 10 ⁵	n/a
HIO ₃	n/a	n/a	n/a	^a 8.0 × 10 ⁴	^e 1.3 × 10 ⁵	n/a	^l 9.0 × 10 ⁴
HO ₂	n/a	2.8 × 10 ¹¹ (RH= 2.5%)	1.2 × 10 ¹¹ (RH=2.7%)	^b 5.2 × 10 ⁵	^g 3.3 × 10 ⁶ (RH =2.7%)	^k 5.7 × 10 ⁵ (RH =0.3%)	n/a
SO ₂	n/a	2.6 × 10 ¹⁶ (RH = 10%)	2.1 × 10 ¹⁶ (RH = 9.9%)	^c 9.4 × 10 ⁷	^h 1.8 × 10 ⁹ (RH = 0.5%)	n/a	n/a
I ₂	n/a	8.2 × 10 ⁹ (RH = 26-37%)	n/a	^d 6.7 × 10 ⁵	^d 3.3 × 10 ⁵	n/a	n/a
IO	n/a	n/a	n/a	^a 3.0 × 10 ⁴	^e 1.6 × 10 ⁵	ⁱ 2.5 × 10 ⁴	n/a
OIO	n/a	n/a	n/a	^a 3.4 × 10 ⁵	^e 2.0 × 10 ⁵	ⁱ 3.1 × 10 ⁴	n/a
I ₂ O ₂	n/a	n/a	n/a	^a 7.9 × 10 ⁴	^e 1.9 × 10 ⁵	ⁱ 3.5 × 10 ⁴	n/a
I ₂ O ₃	n/a	n/a	n/a	^a 4.9 × 10 ⁴	^e 1.9 × 10 ⁵	ⁱ 4.2 × 10 ⁴	n/a
I ₂ O ₄	n/a	n/a	n/a	^a 5.1 × 10 ⁴	^e 1.9 × 10 ⁵	ⁱ 3.0 × 10 ⁴	n/a
I ₂ O ₅	n/a	n/a	n/a	^a 2.5 × 10 ⁵	^e 2.0 × 10 ⁵	ⁱ 3.7 × 10 ⁴	n/a

Unit: molec. cm⁻³ cps cps⁻¹; 'n/a' refer to 'not available'; Experiments were conducted at room temperature. H₂SO₄ calibration factor is applied to estimate the detection limits for the species without direct calibration. The detection limits are estimated with 1-min data and one-hour data collection time. The RH reported in this table is calculated at 25 °C. The calibration factors and LODs have a systematic error of a factor of two (-50%/+100%).

Calibration factors used for the LOD calculation are listed: a. 6.05 × 10⁹, b. 5.03 × 10¹⁰, c. 3.4 × 10¹³, d. 8.2 × 10⁹, e. 8.1 × 10⁹, f. 1.8 × 10¹⁰, g. 2.82 × 10¹¹, h. 1.03 × 10¹⁴, i. 9.8 × 10⁸, j. 5.1 × 10⁹, k. 4.06 × 10¹⁰, l. 3.51 × 10⁹.

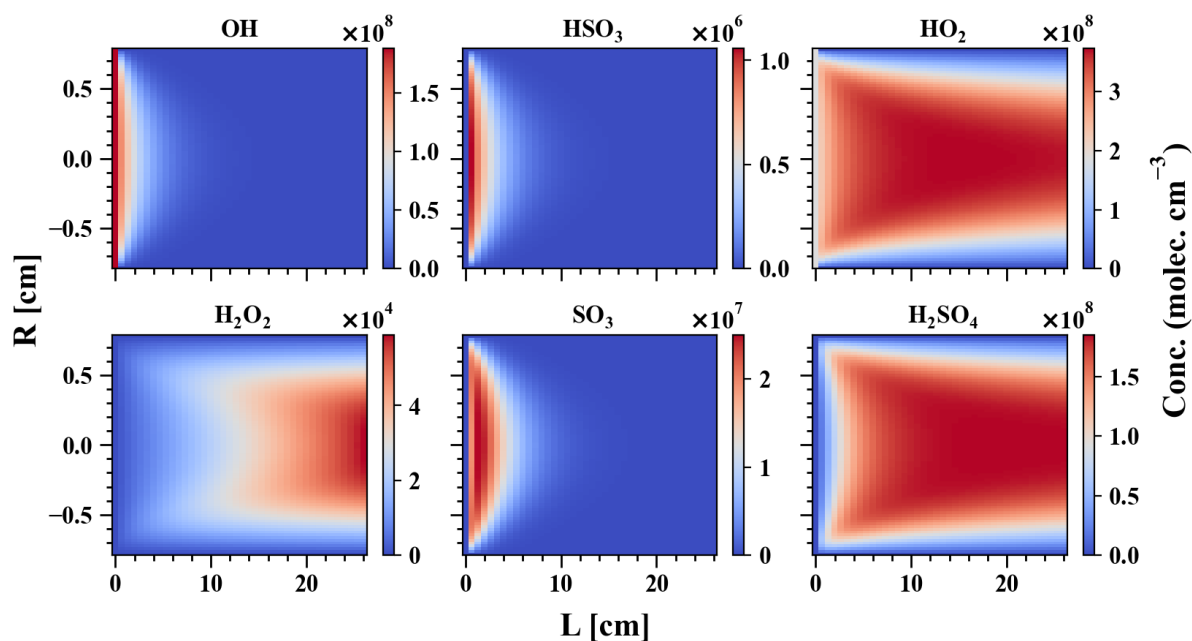


Figure 2. MARFORCE simulation results of the H_2SO_4 calibration. The x-axis shows the distance from the UVP pen-ray lamp to the instrument pinhole and the y-axis shows the distance in the radial direction. Conditions for the simulation: $R = 0.78$ cm, $L = 26$ cm, sample flow = 10.6 slpm, $[\text{SO}_2] = 5.78 \times 10^{13} \text{ cm}^{-3}$, $[\text{O}_2] = 2.42 \times 10^{16} \text{ cm}^{-3}$ and $[\text{H}_2\text{O}] = 2.8 \times 10^{16} \text{ cm}^{-3}$.

The derived calibration factor of Br^- -MION2-T1 (8.1×10^9) is roughly eight times higher than that of Br^- -MION2-T2 (9.8×10^8). This is consistent with that the ionisation time from tower 2 to the pinhole (ca. 300 ms) is approximately 8.6 times longer than that of tower 1 (35 ms). Longer ionisation time results in a larger fraction of Br^- and $\text{H}_2\text{O} \cdot \text{Br}^-$ being converted to $\text{H}_2\text{SO}_4 \cdot \text{Br}^-$ or HSO_4^- , thus a lower calibration factor. As for the NO_3^- -MION2-T1, it achieves a similar sensitivity as the Br^- -MION2-T1 for H_2SO_4 detection. This is likely due to the fact that the ionisation time was kept constant (tower 1 was used) and both the NO_3^- and Br^- chemical ionisation methods measure H_2SO_4 at the collision limit (Kürten et al., 2012; Wang et al., 2021a).

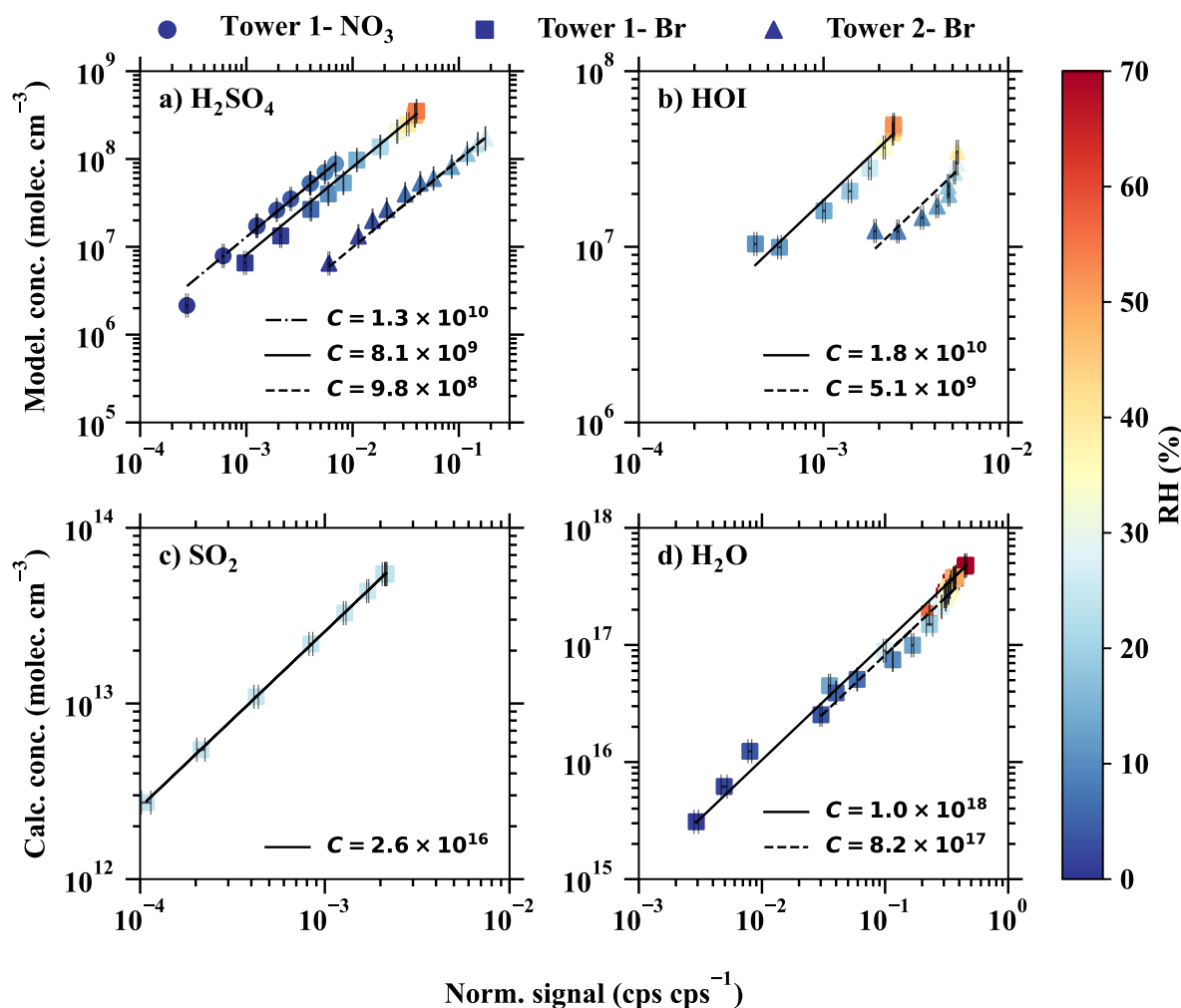


Figure 3. The modelled or calculated vapour concentrations vs. the normalised signals for a) H₂SO₄, b) HOI, c) SO₂, d) H₂O. The dashed-dotted, solid, and dashed lines are the linear fits of the results from different inlet modes: 1) tower 1 with the NO₃⁻ chemical ionisation method, 2) tower 1 with the Br⁻ chemical ionisation method, and tower 2 with the Br⁻ chemical ionisation method. The slopes of the fitted lines represent the calibration coefficients, shown in the legend. The colour bar shows the relative humidity in the calibration experiments.

Sanchez et al. (2016) has reported that the Br⁻-CIMS is capable of detecting HO₂ radicals at ambient relevant concentrations. In this study, we calibrated HO₂ together with H₂SO₄, as HO₂ is a by-product in the chemical production of H₂SO₄ (see supplementary Table A1). As the binding of HO₂ with Br⁻ is significantly weaker than that of H₂SO₄ with Br⁻, the collision induced fragmentation of HO₂·Br⁻ in the ion-optics of the mass spectrometer is larger (Passananti et al., 2019). Additionally, as the humidity effect of HO₂ will be shown to be strong in a section below, the calibration coefficient of HO₂ has to be derived with respect to a specific humidity level. The derived HO₂ calibration factors at 2.5 - 2.7 % RH (25 °C) are 2.8 × 10¹¹ and



345 1.2×10^{11} , respectively, for Br^- -MION2-T1 and Br^- -MION2-T2 (Table 1).

The HOI calibration was also carried out using the H_2SO_4 calibration source, except that the SO_2 source was replaced with an I_2 source. The calibration procedure was described in greater detail in our earlier studies (Tham et al., 2021; Wang et al., 2021a). While the calibration experiment remains the same, the MARFORCE model in this study utilises a complete set of iodine chemistry thus producing a more accurate calibration factor for HOI (supplementary Table A1). We estimate that the
350 HOI concentration using the MARFORCE model is only 0.1 - 0.7 % lower compared to our earlier model which only considers the essential steps of the HOI formation. As can be seen in Figure 3 and Table 1, the calibration factor for HOI is roughly two times that of H_2SO_4 . This suggests that HOI is detected at close to the collision limit. It is worth noting that we find instrument setting affects HOI detection significantly since HOI is not strongly bonded to Br^- . The preferred fragmentation pathway is
355 $\text{HOI} \cdot \text{Br}^- \rightarrow \text{HOI} + \text{Br}^-$ (Table 2), and thus a fraction of $\text{HOI} \cdot \text{Br}^-$ lose the signature of HOI after passing the ion optics of our mass spectrometer. A more fragmentation-oriented setting can result in a higher fraction of $\text{HOI} \cdot \text{Br}^-$ getting lost in the ion optics, thus resulting in a higher calibration factor, i.e., lower sensitivity. As an example, a relatively fragmenting setting was used in our earlier studies in an attempt to reduce $(\text{H}_2\text{O})_n \cdot \text{Br}^-$ clusters and other water-associated clusters which complicated the mass spectra (Tham et al., 2021; Wang et al., 2021a). Such a setting resulted in an eight times higher calibration factor for
360 HOI than that for H_2SO_4 and it cannot be explained by iodine chemistry schemes used in the calibration scripts nor by any differences in the experimental conditions.

3.2 Calibration of H_2O and SO_2

$\text{H}_2\text{O} \cdot \text{Br}^-$ is a regular peak and one of the primary ions measured by the Br^- -CIMS. Br^- -CIMS is, therefore, able to measure absolute water content if the $\text{H}_2\text{O} \cdot \text{Br}^-$ signal is calibrated against a dew point mirror instrument. Such a calibration has at least
365 two purposes: 1) the calibrated $\text{H}_2\text{O} \cdot \text{Br}^- : \text{Br}^-$ can be used as an indicator of the fragmentation level of the Br^- -CIMS and 2) Br^- -CIMS can be more sensitive to H_2O compared with regular relative humidity sensors and dew point mirrors. In this study, the H_2O was calibrated both for the Br^- -MION-T1 and Br^- -MION-T2 as shown in Figure 3. The calibration factors for both of the towers do not differ from each other likely due to the excess amount of H_2O which establishes an equilibrium with Br^- and $\text{H}_2\text{O} \cdot \text{Br}^-$ rapidly regardless of the ionisation time.

370

As a reasonable binding enthalpy of $\text{SO}_2 \cdot \text{Br}^-$ was predicted using quantum chemical calculations (Table 2), we continued to check whether the Br^- -MION2 allows us to detect SO_2 . A variable amount of SO_2 was mixed with a fixed amount of dilution flow at a constant relative humidity (10 %) which was measured by the Br^- -MION2. Clear $\text{SO}_2 \cdot \text{Br}^-$ was measured and it increased linearly with the SO_2 concentration in the sample flow (Figure 3). However, the calibration factor of SO_2 is roughly
375 six orders of magnitude higher than that of H_2SO_4 at 10 % relative humidity (RH). This is consistent with the weaker binding of $\text{SO}_2 \cdot \text{Br}^-$ compared with $\text{H}_2\text{SO}_4 \cdot \text{Br}^-$. Additionally, SO_2 calibration is extremely sensitive to RH changes as can be seen in Figure 4. The best detection limit achieved in this study is $9.4 \times 10^7 \text{ cm}^{-3}$ at below 0.1 % RH and theoretically, it is feasible to further increase the sensitivity by reducing absolute water content.



Table 2. Fragmentation enthalpies (the opposite of binding enthalpies) of analytes with the Br^- . The cluster geometry was optimised at the $\omega\text{B97X-D/aug-cc-pVTZ-PP}$ level of theory at 298.15 K (Chai and Head-Gordon, 2008; Kendall et al., 1992). The enthalpies were calculated at the DLPNO-CCSD(T)/def2-QZVPP at 298.15 K

Cluster fragmentation pathway	Fragmentation enthalpies (kcal mol^{-1})
$\text{I}_2 \cdot \text{Br}^- \longrightarrow \text{I}_2 + \text{Br}^-$	33.3
$\text{I}_2 \cdot \text{H}_2\text{OBr}^- \longrightarrow \text{I}_2 \cdot \text{Br}^- + \text{H}_2\text{O}$	8.0
$\text{IO} \cdot \text{Br}^- \longrightarrow \text{IO} + \text{Br}^-$	24.5
$\text{IO} \cdot \text{H}_2\text{OBr}^- \longrightarrow \text{IO} + \text{H}_2\text{O} \cdot \text{Br}^-$	21.3
$\text{IO} \cdot \text{H}_2\text{OBr}^- \longrightarrow \text{IO} \cdot \text{Br}^- + \text{H}_2\text{O}$	9.9
$\text{OIO} \cdot \text{Br}^- \longrightarrow \text{OIO} + \text{Br}^-$	23.2
$\text{OIO} \cdot \text{H}_2\text{OBr}^- \longrightarrow \text{OIO} + \text{H}_2\text{O} \cdot \text{Br}^-$	22.1
$\text{OIO} \cdot \text{H}_2\text{OBr}^- \longrightarrow \text{OIO} \cdot \text{Br}^- + \text{H}_2\text{O}$	11.9
$\text{I}_2\text{O}_3 \cdot \text{Br}^- \longrightarrow \text{IO}_3^- + \text{IBr}$	24.6
$\text{I}_2\text{O}_4 \cdot \text{Br}^- \longrightarrow \text{I}_2\text{O}_4 + \text{Br}^-$	42.6
$\text{I}_2\text{O}_4 \cdot \text{H}_2\text{OBr}^- \longrightarrow \text{I}_2\text{O}_4 + \text{H}_2\text{O} \cdot \text{Br}^-$	48.8
$\text{I}_2\text{O}_4 \cdot \text{H}_2\text{OBr}^- \longrightarrow \text{I}_2\text{O}_4 \cdot \text{Br}^- + \text{H}_2\text{O}$	10.5
$\text{HIO}_3 \cdot \text{Br}^- \longrightarrow \text{IO}_3^- + \text{HBr}$	^a 29.9
$\text{HIO}_3 \cdot \text{Br}^- \longrightarrow \text{HIO}_3 + \text{Br}^-$	^a 35.7
$\text{HIO}_3 \cdot \text{H}_2\text{OBr}^- \longrightarrow \text{HIO}_3 + \text{H}_2\text{O} \cdot \text{Br}^-$	33.1
$\text{HIO}_3 \cdot \text{H}_2\text{OBr}^- \longrightarrow \text{HIO}_3 \cdot \text{Br}^- + \text{H}_2\text{O}$	11.2
$\text{HIO}_3 \cdot \text{H}_2\text{OBr}^- \longrightarrow \text{IO}_3 \cdot \text{H}_2\text{O}^- + \text{HBr}$	26.7
$\text{HIO}_2 \cdot \text{Br}^- \longrightarrow \text{HIO}_2 + \text{Br}^-$	^b 29.2
$\text{HIO}_2 \cdot \text{H}_2\text{OBr}^- \longrightarrow \text{HIO}_2 + \text{H}_2\text{O} \cdot \text{Br}^-$	15.5
$\text{HIO}_2 \cdot \text{H}_2\text{OBr}^- \longrightarrow \text{HIO}_2 \cdot \text{Br}^- + \text{H}_2\text{O}$	1.3
$\text{HIO}_2 \cdot \text{H}_2\text{OBr}^- \longrightarrow \text{IO}_2 \cdot \text{H}_2\text{O}^- + \text{HBr}$	27.4
$\text{HOI} \cdot \text{Br}^- \longrightarrow \text{HOI} + \text{Br}^-$	^b 26.9
$\text{HOI} \cdot \text{H}_2\text{OBr}^- \longrightarrow \text{HOI} + \text{H}_2\text{O} \cdot \text{Br}^-$	22.9
$\text{HOI} \cdot \text{H}_2\text{OBr}^- \longrightarrow \text{HOI} \cdot \text{Br}^- + \text{H}_2\text{O}$	9.6
$\text{HOI} \cdot \text{H}_2\text{OBr}^- \longrightarrow \text{IO} \cdot \text{H}_2\text{O}^- + \text{HBr}$	48.4
$\text{H}_2\text{O} \cdot \text{Br}^- \longrightarrow \text{H}_2\text{O} + \text{Br}^-$	13.2
$\text{HO}_2 \cdot \text{Br}^- \longrightarrow \text{HO}_2 + \text{Br}^-$	23.1
$\text{H}_2\text{SO}_4 \cdot \text{Br}^- \longrightarrow \text{HSO}_4^- + \text{HBr}$	^b 27.9
$\text{H}_2\text{SO}_4 \cdot \text{H}_2\text{OBr}^- \longrightarrow \text{H}_2\text{SO}_4 + \text{H}_2\text{O} \cdot \text{Br}^-$	36.1
$\text{H}_2\text{SO}_4 \cdot \text{H}_2\text{OBr}^- \longrightarrow \text{H}_2\text{SO}_4 \cdot \text{Br}^- + \text{H}_2\text{O}$	8.2
$\text{H}_2\text{SO}_4 \cdot \text{H}_2\text{OBr}^- \longrightarrow \text{HSO}_4 \cdot \text{H}_2\text{O}^- + \text{HBr}$	22.0
$\text{SO}_2 \cdot \text{Br}^- \longrightarrow \text{SO}_2 + \text{Br}^-$	19.4

^athe fragmentation enthalpy is updated from Wang et al. (2021a) as a lower energy $\text{HIO}_3 \cdot \text{Br}^-$ cluster geometry, which has an additional Br-I interaction, has been located in this study (see supplementary Figure A6). ^bValue adopted from Wang et al. (2021a).

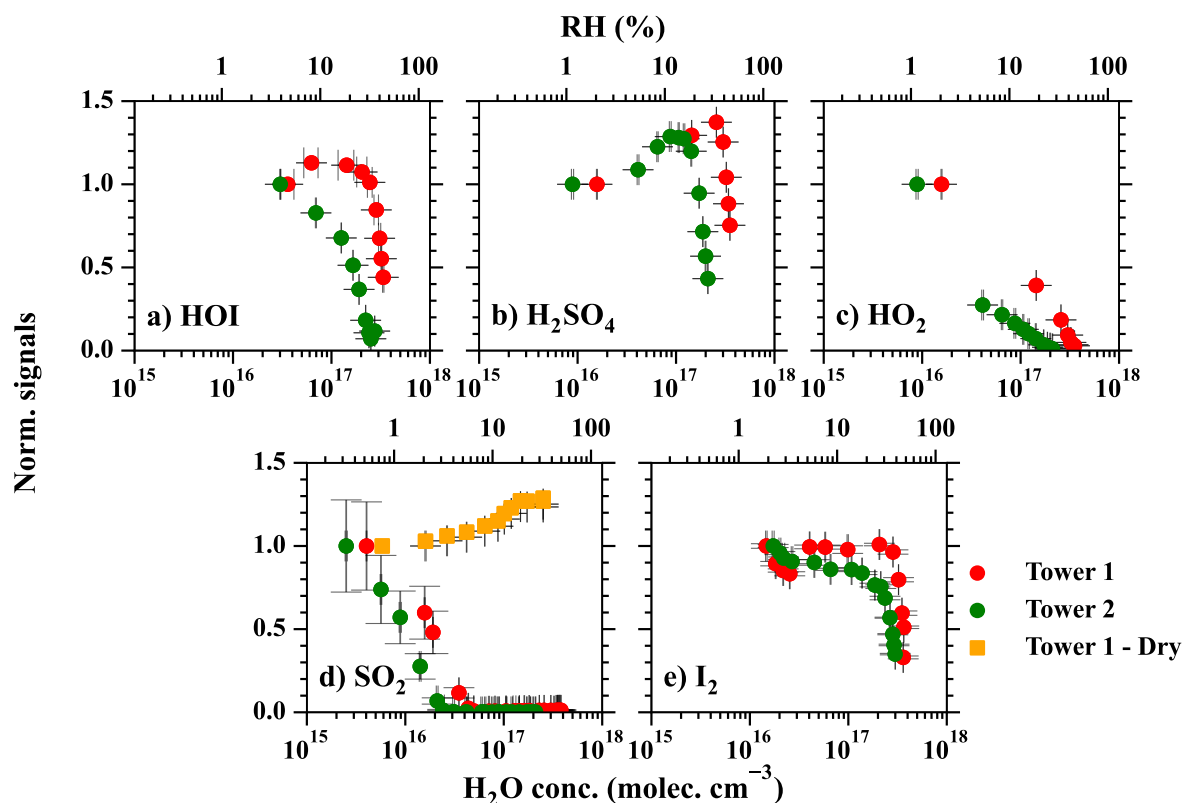


Figure 4. The effect of humidity on the detection efficiency of a) HOI, b) H_2SO_4 , c) HO_2 , d) SO_2 , and e) I_2 . The measured signals in each set of experiments are normalised by the signal at the lowest RH. Therefore, the normalised signals represent how the increasing RH is affecting the detection limit compared with the initial point. The red and green circles show the detection humidity effects of tower 1 and tower 2, respectively. The yellow squares refer to the experiments conducted with a dry flow added before the MION2 inlet. The RH is converted from absolute H_2O concentrations at 25°C . Error bars represent one standard deviation.

3.3 Detection humidity effect

380 The measurement sensitivity of halide ion based chemical ionisation method was regularly reported to be affected by atmospheric water content (Kercher et al., 2009; Mielke et al., 2011; Woodward-Massey et al., 2014; Lee et al., 2014). The humidity effect of atmospheric pressure Br^- -MION2 could be even stronger owing to the higher water content in the air samples. Although our earlier study has demonstrated that the detection of I_2 by Br^- -MION1 was not affected within a limited humidity variation (40 - 80 % RH at -10°C), characterisation under a wider range of humidity conditions is needed. As the detection
385 humidity effect in this study exclusively refers to the effect of absolute humidity instead of relative humidity, absolute humidity parameters such as dew/frost point or H_2O molecule concentration are commonly presented together with the relative humidity (at 25°C , otherwise notified).



In this study, we examine the detection humidity effect of H_2SO_4 , HOI , HO_2 , SO_2 and I_2 with RH from below 1 % to 60 % at
390 25 °C. The detection humidity effect of SO_2 and I_2 is relatively easier to characterise as the calibration source is not involved.
Therefore, a straight flow reactor is used to premix the analyte containing air sample to the Br^- -MION2 (Figure A2). It is worth
noting that we do not account for the wall loss of SO_2 and I_2 in the analysis. The wall loss of SO_2 is negligible at the time
scale of the calibration processes (few seconds). Despite I_2 being a sticky gas which both condenses to and evaporates from
the wall of the flow reactor, an equilibrium can be reached if given sufficient time. When equilibrium is reached, which could
395 take up to 24 hours in our experiments, the condensation and evaporation of I_2 cancel each other out and thus the estimation of
 I_2 concentration is straightforward.

On the other hand, the characterisation of the detection humidity effect of H_2SO_4 , HOI and HO_2 is more challenging as
the production of these species is nearly proportional to the amount of H_2O passing the calibration source. Therefore, an ex-
400 perimental apparatus was built which enabled humidifying the air sample after the calibrator, thus without disturbing HO_x
production processes in the calibration source (Figure A3).

The results of the humidity characterisation are shown in Figure 4. Despite distinct humidity sensitivity is observed for the
mentioned five species, a general conclusion can be drawn for essentially all of the species - an excess amount of water content
405 results in lower detection sensitivity. The species with stronger binding with Br^- exhibits higher tolerance to humidity changes
(e.g. H_2SO_4 , I_2 and HOI), while the weakly bonded ones (SO_2 and HO_2) are strongly affected. The humidity tolerance of the
measured species can be ordered as $\text{I}_2 > \text{HOI} > \text{HO}_2 > \text{SO}_2$ which is the same order as the strength of their bindings with Br^-
(Table 2).

410 Interestingly, the detection humidity effect of H_2SO_4 is observed to be non-linear, i.e., the detection sensitivity of H_2SO_4 first
increases with higher RH but eventually has a sharp drop at around 40 % RH (25 °C). The enhancement of H_2SO_4 detection
at below ca. 33 % RH could be contributed by two mechanisms. First, the diffusivity of H_2SO_4 is lower at higher RH (Hanson
and Eisele, 2000). A higher RH, therefore, reduces the wall deposition of H_2SO_4 in the inlet tube, thus effectively increasing
the detected H_2SO_4 . This is a universal systematic error which affects any H_2SO_4 detection technique with appreciable sam-
415 pling line residence time. The second possibility is that at low RH regime, H_2O does enhance H_2SO_4 detection by offering
more modes through which the excess energy of the cluster can dissipate in the formation of $\text{H}_2\text{SO}_4 \cdot \text{Br}^-$, thus resulting in a
relatively more stable cluster (Iyer et al., 2017). Regardless of the sources of the detection humidity effect at the low water
content regime, the maximum systematic error is measured to be 37 % by comparing the experiment carried out at 2 % RH
(frost point of -25 °C) and the experiment carried out at 33 % (dew point of 7.6 °C) in Figure 4b. As the humidity change in
420 ambient conditions is commonly smaller than during experiments, we expect that the detection humidity effect of H_2SO_4 is
moderate when the dew point is below ca. 7.6 °C.



Additionally, a longer reaction time in the ion-molecule reaction chamber by utilising the Br^- -MION2-T2 results in a stronger detection humidity effect as shown in Figure 4. Although such an effect is difficult to quantify, it practically suggests
425 that the Br^- chemical ionisation method should employ a shorter ionisation time when operating MION2 with multiple chemical ionisation methods.

In summary, we find that the detection of Br^- -MION2 is strongly affected by air water content. The atmospheric pressure
 Br^- chemical ionisation method is suitable for laboratory experiments where water content is controlled and atmospheric ob-
430 servations in the cryosphere where air water content is low. Nevertheless, the humidity effect should be considered individually for different analytes and the binding enthalpy between the analyte and Br^- is likely a good indicator. As the NO_3^- -MION2 (or the NO_3^- chemical ionisation, in general, is known to have minimal detection humidity sensitivity, it is commonly operated together with the Br^- -MION2. Cross-check of mutually measured species (e.g., H_2SO_4 , HIO_3 and oxidised organic species) will give essential information on whether and when the Br^- -MION2 detection is compromised by air water content. In this
435 regard, the new design of Br^- -MION2 allowing as many as three chemical ionisation methods to have the same ionisation time is essential.

3.4 Attempts to reduce the detection humidity effect

Several ways were explored to reduce the detection humidity effect. The first and usual way of reducing the detection humidity effect is deploying a low-pressure chemical ionisation system which was regularly used for, e.g., iodide chemical ionisation
440 systems (Lee et al., 2014) or bromide chemical ionisation systems (Wang et al., 2021a). However, the reduction of air sample RH is at the cost of reducing measurement sensitivity, as the air sample is unavoidably diluted. We estimated previously that the Br^- -FIGAERO inlet had more than 10 times higher detection limit compared to the Br^- -MION1 inlet (Wang et al., 2021a). For example, the Br^- -FIGAERO had an HIO_3 detection limit of $5.1 \times 10^6 \text{ cm}^{-3}$ which struggles to detect atmospheric level of HIO_3 (commonly below 10^7 cm^{-3}) (He et al., 2021b). The lower level of detection limit provided by the Br^- -MION2 inlet is
445 therefore essential in the detection of iodine species. Another important factor is the reaction of halogen radicals with analytes. Besides halogen anions, halogen radicals can also be produced by chemical ionisation processes. While iodine radical ($\text{I}\cdot$) mostly reacts with halogen species and a very limited number of organic species, bromide radical ($\text{Br}\cdot$) reacts with a wider range of organic species as it has a larger reactivity. Regular low-pressure systems which mix analyte with reagent gases (e.g., FIGAERO inlet) may introduce an additional complexity when interpreting measured mass spectra. Therefore, we had to seek
450 alternatives to help reduce the detection humidity effect.

The first method is the dilution method. Instead of measuring the air sample directly, a dry dilution flow was mixed with the air sample at the entrance of the Br^- -MION2 inlet (see supplementary Figure A4). We tested this method for the SO_2 detection with an air sample flow of 1.8 slpm and a dilution flow of 20.7 slpm (Figure 4). The x-axis for this set of experiments represents
455 humidity in the air sample instead of the humidity after the dilution to compare with the experiments without adding the dilution flow. We observe a significantly reduced detection humidity effect compared to the case without dilution. It is noteworthy



460 that as the air sample is diluted by a factor of 21.5, the detection limit of the instrument is likely enhanced by the same factor. However, since the detection humidity effect for SO_2 is significantly higher than other species (e.g., H_2SO_4 , HOI and I_2), the dilution is still effective for SO_2 measurement. For example, no $\text{SO}_2 \cdot \text{Br}^-$ signal would be measured at 40 % RH (25 °C) if the air sample is not diluted but a noticeable signal would be measured if the air sample is diluted. A similar conclusion is likely applicable to other species but with a different optimal humidity cut-off.

465 The second method is additionally introducing a core-sampling device that uses the air sample as the core flow and a dry synthetic air flow as the sheath flow (supplementary Figure A9). This takes the advantage of the fact that H_2O diffuses into the sheath flow faster than other analytes with larger molecular weight, thus effectively reducing the RH in the core flow from which the instrument pinhole collects the most sample. On the other hand, the core-sampling method also inevitably reduces the $\text{SO}_2 \cdot \text{Br}^-$ signal as SO_2 also gets diluted which partially counters the reduced detection humidity effect. Various sample-to-sheath flow combinations were tested as presented in Figure 5. To compare the SO_2 detection coefficient to standard conditions, the measured $\text{SO}_2 \cdot \text{Br}^-$ signal from all sets of experiments is normalized by the experiment with the sample-to-sheath ratio of 21:1 at 0.21 % RH (25 °C). The results reveal that reducing the sample-to-sheath ratio effectively eases the SO_2 detection humidity effect. The results show that different mixing ratios only moderately affect the measured $\text{SO}_2 \cdot \text{Br}^-$ when H_2O is smaller than 10^{16} cm^{-3} (1 % RH; the detection humidity effect remains low). This is likely due to the fact that the instrument pinhole primarily measures the air sample in the core flow, as it only sucks 0.8 slpm. However, the core-sampling device clearly enhances the SO_2 detection efficiency when the H_2O concentration is larger than 10^{16} cm^{-3} . The sample-to-sheath ratio of 1:21 enables effective detection of SO_2 at around $4.5 \times 10^{17} \text{ cm}^{-3}$ (60 % RH) of H_2O while the sample-to-sheath ratio of 21:1 is not able to detect SO_2 after around $4.3 \times 10^{16} \text{ cm}^{-3}$ of H_2O (6 % RH). Overall, the sample-to-sheath ratio of 21:1 is at least two orders of magnitude more effective in detecting SO_2 when H_2O is greater than 10^{16} cm^{-3} . Therefore, the core-sampling method is an effective method for reducing the detection humidity effect of species which are weakly bonded with Br^- . However, since the detection limit is nevertheless changed by the sample water content, dedicated experiments have to be carried out to derive the concentration of the analyte (e.g., SO_2).

470
475
480

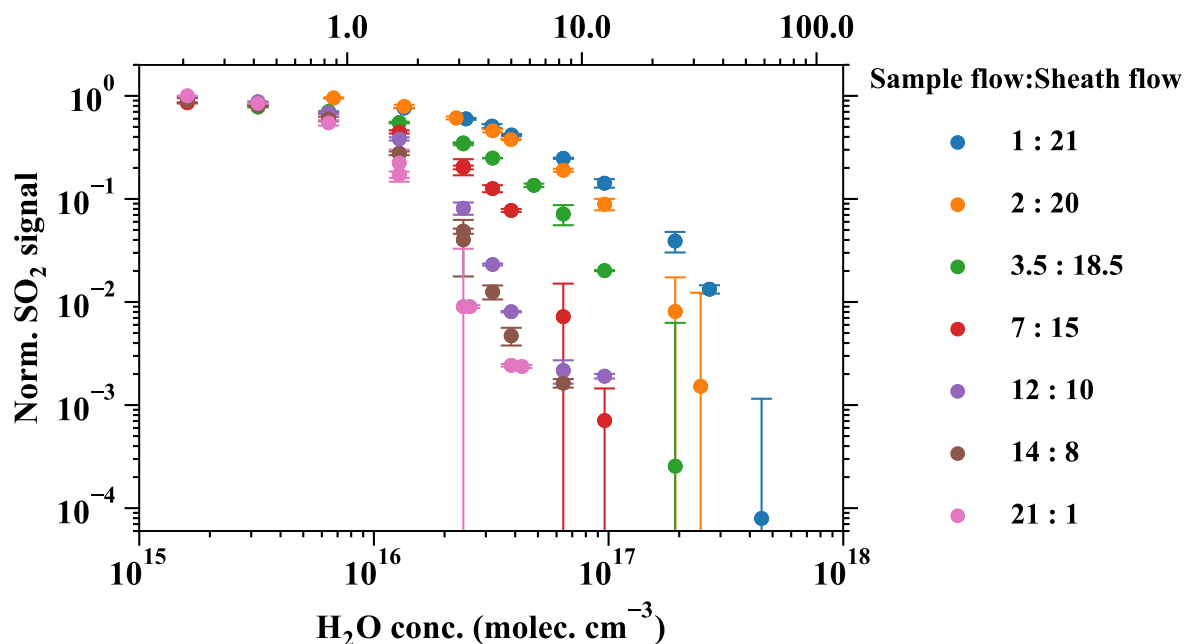


Figure 5. Reducing the detection humidity effect with the core sampling method (supplementary Figure A9). This design takes the advantage of the faster diffusion of H₂O than SO₂ from the sample flow to the sheath flow and effectively reduces the RH in the sample flow. Various sample-to-sheath ratios were tested at different H₂O concentrations to find the optimal setting. All the data are normalised to the lowest RH data point in the sample-to-sheath = 21:1 experiment. Due to experimental constraints, the sample-to-sheath ratios = a) 3.5:18.5, b) 2:20 and c) 1:21 experiments started only from the second, third and fourth lowest RH points, respectively. All other experiments collected data in all humidity conditions. The error bars represent the standard deviation of the normalised SO₂ signals.

3.5 Limit of detection

The limit of detection (LOD) is an essential parameter for a chemical ionisation inlet system. For the convenience of inter-comparison, we define the LOD in this study as:

$$\text{LOD} = \mu + 3 \times \sigma \quad (3)$$

485 where μ is the mean value of one-hour mass spectrometric data with a one-minute time resolution and σ is the standard variation of the same data. Both μ and σ include the experimentally derived calibration coefficient. The species without direct calibration utilise the calibration coefficient of H₂SO₄, thus the LODs for these species generally represent the lower limit. The LODs are measured by passing pure nitrogen or synthetic air to the chemical ionisation inlet in which case none of the species listed in Table 1 is expected. It should be noted that this LOD definition is suitable for disentangling trace gas concentrations

490 from background levels in long-term observations. Values above the LOD can commonly be distinguished from the time series. If one does a careful analysis of the measured mass spectra, a lower value may be recognised.



The reported LODs can be affected by many factors. Some of these factors are 1) the purity of the reagent source (e.g., nitric acid solution and dibromomethane solution), 2) the purity of the sample air used at the LOD determination experiment, 3) the signal-to-noise (electronic background noise) ratio of the instrument, 4) the softness of the tuning of the mass spectrometer, and 5) the humidity of the sample air used at the LOD determination experiment (for Br^- chemical ionisation).

Due to the complex nature of the LOD determination, the MION2 inlet was coupled with two independent mass spectrometers (APi1 and APi2, respectively, see Table 1) to test its robustness. The LOD determination experiments were carried out with APi1 and APi2 in two independent laboratory environments with independent reagent sources and sample air. These two instruments were also individually tuned, thus having different signal-to-noise ratios and fragmentation levels. The results of the LOD determination experiments are tabulated in Table 1. Both of the Br^- -MION2-T1-APi1 and Br^- -MION2-T1-APi2 achieved LODs at the level of 10^5 cm^{-3} for species that are detected at the collision limit (e.g., H_2SO_4 , I_2 and HIO_3). In general, the Br^- -MION2-T1-APi2 has a slightly lower LOD compared with Br^- -MION2-T1-APi1. This could result from the fact that the APi1 has not been serviced for more than four years by the point of the experiments and the multi-channel plate could have degraded.

It is worth noting that it may appear that the H_2SO_4 and I_2 LODs of MION2-T1 ($1 \times 10^5 \text{ cm}^{-3}$ and $3.3 \times 10^5 \text{ cm}^{-3}$) are similar to that reported for MION1-T1 ($2 \times 10^5 \text{ cm}^{-3}$ and $3.8 \times 10^5 \text{ cm}^{-3}$) in our earlier study (Wang et al., 2021a). This is because the mass spectrometer used in Wang et al. (2021a) (noted as APi3) had a higher signal-to-noise ratio compared with the APi1. Therefore, getting similar LODs from the MION2-T1-APi1 and MION1-T1-APi3 already suggests that the MION2 inlet has improved its performance. In order to avoid this systematic error, we additionally compared the H_2SO_4 LOD of the MION2 inlet with that of the Eisele-type inlet, both attached to the APi1 (Table 1). The direct comparison suggests that the MION2-T1 LOD is roughly 30 % higher than the LOD of the widely-used Eisele inlet, thus a comparable performance. When we increased the ionisation time from 35 ms (MION2-T1) to 300 ms (MION2-T2), the LOD of MION2 for H_2SO_4 is further reduced by a factor of three, thus MION2-T2 performs better than the Eisele inlet. This suggests that the MION2 inlet achieves comparable (MION2-T1) or even better (MION2-T2) LODs than the Eisele inlet. Additional tuning of the ionisation time may further increase the advantage for chemical ionisation methods that are less affected by air water content (e.g., NO_3^- -CIMS).

Additionally, the Eisele-type inlet was regularly shown to have LODs as low as 10^4 cm^{-3} (Jokinen et al., 2012), a well-performing mass spectrometer will likely further reduce the LODs of MION2. Nevertheless, the achieved LODs are low enough for atmospheric measurements as the discussed molecules commonly need to be above 10^6 cm^{-3} to have a significant impact on atmospheric chemistry and aerosol formation.

3.6 Voltage scanning and cluster formation enthalpy

Collision induced cluster fragmentation is an unavoidable issue which affects the detection of analytes that are weakly bonded with the reagent ion. Since if a charged cluster is loosely bonded, collisions between charged clusters and air molecules in

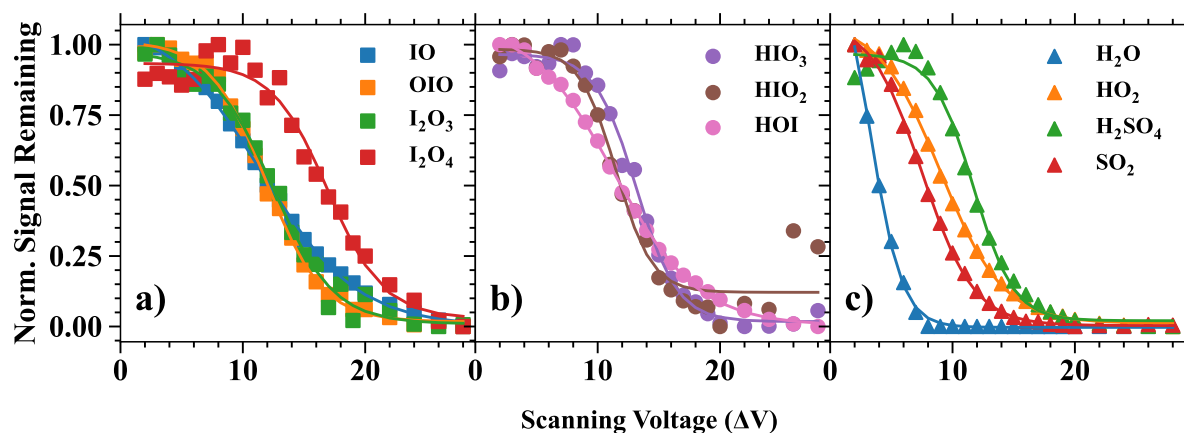


Figure 6. Normalised signal remaining vs. the scanning voltage (ΔV). The normalised signal remaining of each species is normalised by the maximum and minimum values of its values with different ΔV . The ΔV describes the voltage difference between the skimmer and the second quadrupole and can be considered an indicator of the softness of the instrument tuning (Lopez-Hilfiker et al., 2016). A higher ΔV commonly indicates a more fragmenting setting.

the atmospheric pressure interface may break a large portion of the charged clusters apart prior to reaching the detector (Pasananti et al., 2019). Therefore, charged cluster binding strength is an important factor determining whether an analyte-charger ion cluster can be measured by the mass spectrometer (Iyer et al., 2016; Lopez-Hilfiker et al., 2016; Wang et al., 2021a).
530 Lopez-Hilfiker et al. (2016) has shown that the level of collision induced cluster fragmentation is associated with the voltage differences between the first and second quadrupoles in the atmospheric pressure interface of the mass spectrometer. The voltage difference was shown to be indicative of the fragmentation level of the CIMS and it positively correlates with the cluster formation enthalpy (Iyer et al., 2016).

535 In this study, we carried out voltage scan experiments with the same procedures as described in Lopez-Hilfiker et al. (2016). Briefly, we kept the voltage differences inside two individual quadrupoles constant while changing the voltage difference between these two quadrupoles to modulate energies in the collision processes and the results are shown in Figure 6. Generally, a higher voltage difference indicates a higher fragmentation level which in turn results in a lower remaining fraction of charged clusters. Charged clusters that are less sensitive to voltage changes, especially in the low voltage difference regime (e.g., ΔV
540 < 10 V), are more stable.

A series of iodine oxides and oxoacids is evaluated together with other inorganic species such as H_2O , HO_2 , SO_2 and H_2SO_4 (Figure 6). Based on the results, we categorise the analytes into three categories: 1) analytes which are strongly bonded with Br^- , 2) analytes which are moderately bonded with Br^- and 3) analytes which are weakly bonded with Br^- . H_2SO_4 , HIO_3 ,
545 HIO_2 and I_2O_4 clearly fall into the first category as the initial change of voltage difference does not affect the normalized signal



550 significantly, i.e., they are detected at the collision limit. It is also apparent that H_2O , HO_2 and SO_2 belong to the third category since a small increase in the voltage difference leads to substantially reduced normalised ratios. Finally, IO, OIO, I_2O_3 and HOI are moderately bonded with Br^- . These moderately bonded charged clusters reach a close to collision limit detection if the instrument is softly tuned (the voltage difference is small) but their detection sensitivity can change dramatically if the instrument fragmentation level is high.

555 Additionally, formation free enthalpies of various charged clusters are calculated using quantum chemical calculations (see Methods) and are compared with the voltages at which 50 % of the charged clusters dissociate (ΔV_{50}) as shown in Figure 7. These two sets of parameters are theoretical predictions and measurements of the binding strength and they show a consistent picture, as shown previously and in this study (Lopez-Hilfiker et al., 2016; Iyer et al., 2016). As a summary, strongly bonded charged clusters have larger fragmentation free enthalpies, larger ΔV_{50} values and a lower calibration factor (e.g., $\text{H}_2\text{SO}_4 \cdot \text{Br}^-$, $\text{I}_2 \cdot \text{Br}^-$). The weakly bonded charged clusters have the opposite properties (e.g., $\text{HO}_2 \cdot \text{Br}^-$, $\text{H}_2\text{O} \cdot \text{Br}^-$ and $\text{SO}_2 \cdot \text{Br}^-$).

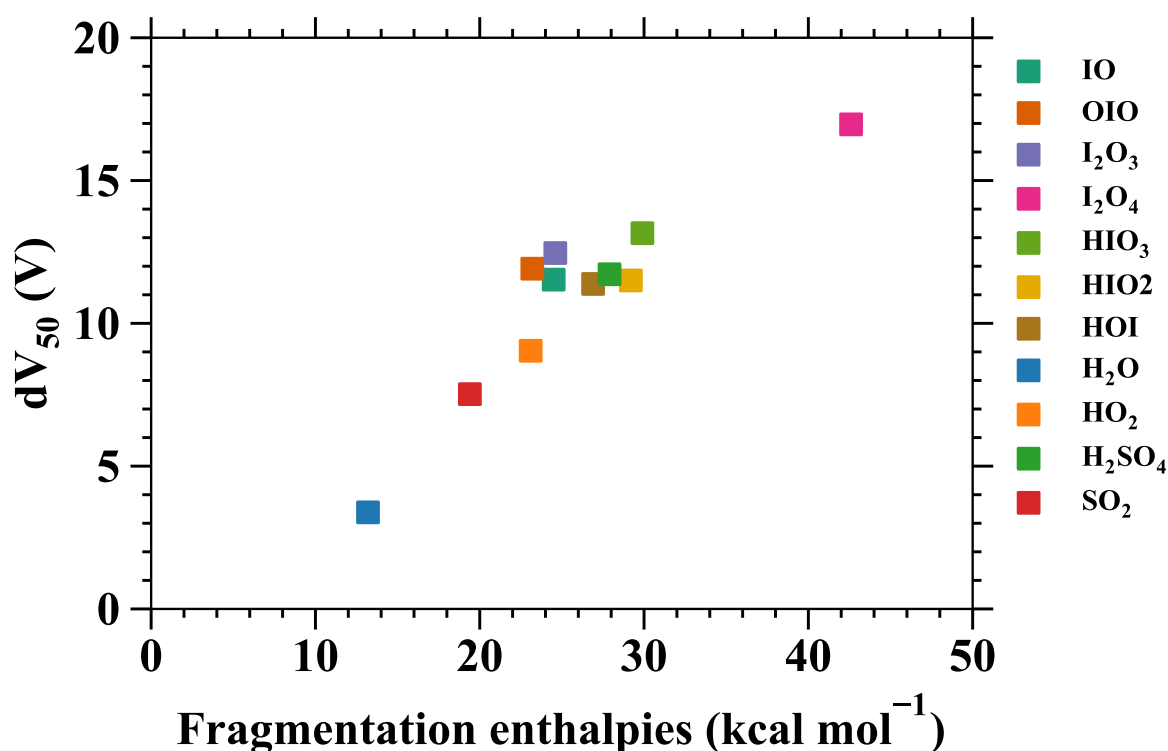


Figure 7. The voltage at which 50 % of analyte-bromide adducts have dissociated (ΔV_{50}) vs. the fragmentation free enthalpies of the adducts (Table 2).



3.7 Validation of the measurement of iodine-containing species

Oxidised iodine vapours have been shown to influence atmospheric oxidation capacity (Sherwen et al., 2016; Wang et al., 2021b) and particle formation processes (Hoffmann et al., 2001; O'Dowd et al., 2002). Recent publications have suggested iodine oxoacids as the critical driver for iodine particle formation processes (Sipilä et al., 2016; Baccarini et al., 2020; He et al., 2021b, a; Zhang et al., 2022; Liu et al., 2023). However, active debate remains concerning the presence of gaseous HIO₃ and whether HIO₃ plays an important role in atmospheric aerosol nucleation. For example, a recent laboratory study shed doubts on the existence of gaseous HIO₃ as the authors only managed to measure HIO₃ in the particle phase with a photoionisation mass spectrometer but not in the gas phase. They concluded that the particle phase HIO₃ was formed from higher iodine oxides, I₂O_y, instead of from gaseous HIO₃ (Gómez Martín et al., 2020). Additionally, they hypothesised that the IO₃⁻ signal, which was previously interpreted as part of the gaseous HIO₃ measured by the NO₃⁻-CIMS (Sipilä et al., 2016), could also originate from I₂O_y. Their evidence is primarily the exothermicity of the I₂O_y reactions with NO₃⁻ which forms IO₃⁻ as part of the products. However, it should be noted that exothermic reactions do not guarantee that the reactions occur at significant rates. For example, reactions such as

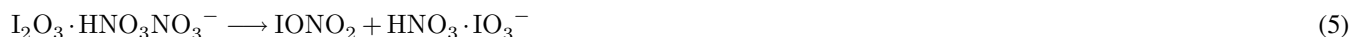


involves breaking several strong I-O and N-O bonds that are likely associated with high kinetic barriers and one could expect that this reaction does not occur as fast as the HIO₃ + NO₃⁻ → IO₃⁻ + HNO₃ reaction, in which case only one proton transfer reaction occurs.

575

It is worthwhile to note that both our earlier studies (He et al., 2021b; Finkenzeller et al., 2022) and (Gómez Martín et al., 2020, 2022) concluded that I₂O₄ is the primary form of I₂O_y. Fortunately, gaseous I₂O₄ is well measured by both the NO₃⁻ and Br⁻ chemical ionisation methods. Finkenzeller et al. (2022) calculated the cluster formation enthalpy of I₂O₄·NO₃⁻ as -45.6 kcal mol⁻¹, which indicates that the I₂O₄·NO₃⁻ cluster is extremely stable. Gómez Martín et al. (2020) found that the I₂O₄ + NO₃⁻ → products + IO₃⁻ reaction is endothermic thus less likely to occur. The same also applies to the Br⁻ chemical ionisation method. As already discussed in the last section, voltage scan experiments indicate that the I₂O₄·Br⁻ cluster is in fact the most stable cluster among the examined clusters (see Figure 7). Therefore, I₂O₄ is detected at the collision limit with the Br⁻ chemical ionisation method and it does not fragment into species such as IO₃⁻.

585 In a more recent study, Gómez Martín et al. (2022) alternatively used the nitrate chemical ionisation method and detected gaseous HIO₃, thus confirming our earlier studies (Sipilä et al., 2016; He et al., 2021b, a) of the existence of gaseous HIO₃. However, the authors additionally suggested that the measured HIO₃·NO₃⁻ ion, which was interpreted as HIO₃ could also be formed from reactions such as below:





590 due to the reaction being exothermic. Besides the same reasons noted above, this hypothesis is challenged by the fact that the
reaction



is a favoured pathway compared to the reaction 5 as shown in Figure 8. We further estimate that the MESMER derived overall
rate coefficients at 298 K, 1 atm for reactions 5 and 6 and they are $2.3 \times 10^{-12} \text{ cm}^3 \text{ molec}^{-1} \text{ s}^{-1}$, and $1.26 \times 10^{-9} \text{ cm}^3 \text{ molec}^{-1}$
595 s^{-1} , respectively. Therefore, the yield of the reaction 6 is close to unity and cannot affect the HIO_3 detection.

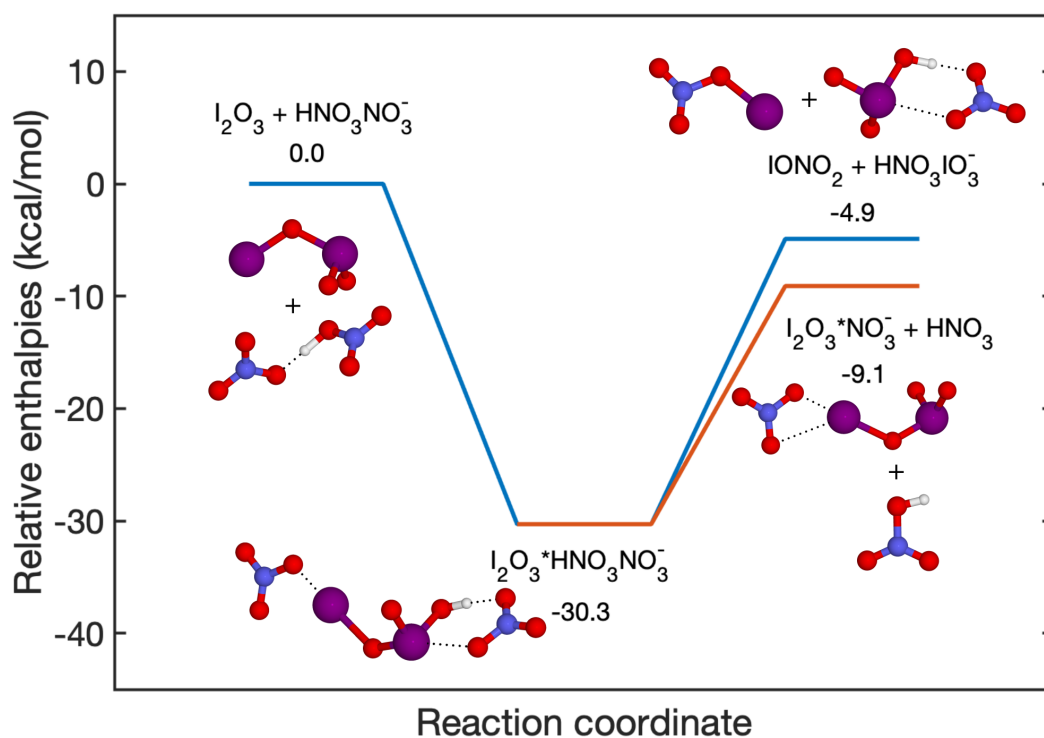


Figure 8. Fragmentation pathways of $\text{I}_2\text{O}_3 \cdot \text{HNO}_3\text{NO}_3^-$. The enthalpies are calculated at the DLPNO-CCSD(T)/def2-QZVPP//wb97X-D/aug-cc-pVTZ-PP level of theory.

Most importantly, higher iodine oxides and iodine oxoacids are formed through complex and distinct chain reactions. Laboratory experiments with elevated iodine concentrations could inevitably disturb the ratio of iodine oxides to iodine oxoacids. The concentration of iodine monoxide (IO) is commonly considered a good indicator of the intensity of atmospheric iodine
600 activities and was shown to influence the ratio of I_xO_y and HIO_x (Finkenzeller et al., 2022). We took advantage of this phenomenon and carried out chemical perturbation experiments by varying O_3 while keeping I_2 concentration and light intensity



constant in a laminar flow reactor. The experiments were repeated for both the Br^- -MION2-T1 and NO_3^- -MION2-T1 shown in Figure 9. The measured IO_3^- signal is compared with $\text{HIO}_3 \cdot \text{NO}_3^-$ from the NO_3^- -MION2-T1 and to $\text{HIO}_3 \cdot \text{Br}^-$, $\text{I}_2\text{O}_3 \cdot \text{Br}^-$ and $\text{I}_2\text{O}_4 \cdot \text{Br}^-$ from the Br^- -MION2-T1 to find out the origin of IO_3^- . Interestingly, the gaseous HIO_3 signals ($\text{HIO}_3 \cdot \text{NO}_3^-$ and $\text{HIO}_3 \cdot \text{Br}^-$) are perfectly linear with the IO_3^- signals, while the $\text{I}_2\text{O}_3 \cdot \text{Br}^-$ and $\text{I}_2\text{O}_4 \cdot \text{Br}^-$ show non-linear dependence on IO_3^- . This suggests that the primary source of IO_3^- is gaseous HIO_3 , since if I_2O_y does contribute to IO_3^- , a non-linear correlation between $\text{HIO}_3 \cdot \text{NO}_3^-$ and $\text{HIO}_3 \cdot \text{Br}^-$ with IO_3^- would be expected.

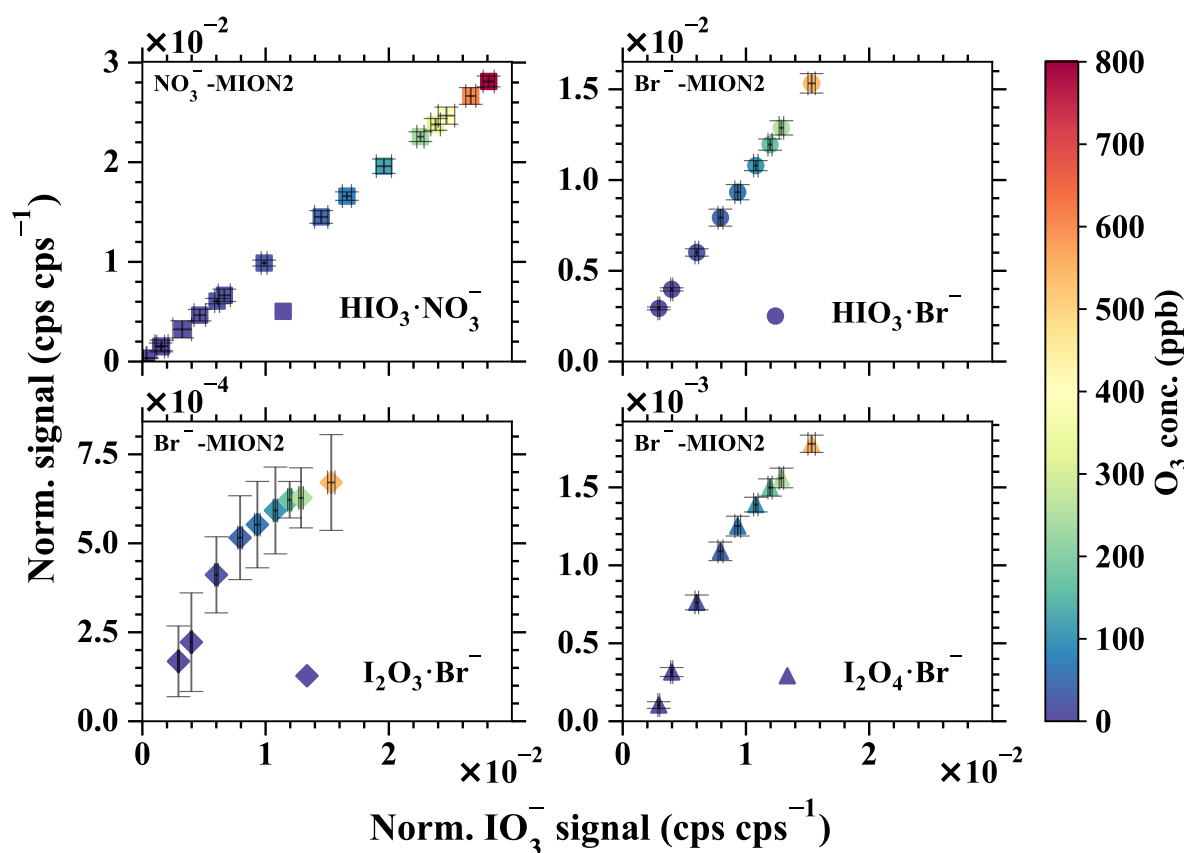


Figure 9. The normalised IO_3^- signal vs. the normalised signals of a) $\text{HIO}_3 \cdot \text{NO}_3^-$, b) $\text{HIO}_3 \cdot \text{Br}^-$, c) $\text{I}_2\text{O}_3 \cdot \text{Br}^-$, and d) $\text{I}_2\text{O}_4 \cdot \text{Br}^-$. The iodine injection and light intensity were kept constant but the O_3 concentration was varied to modulate the ratio of iodine oxides to oxoacids. Error bars show one standard deviation. Notice the different y-axis scales.

In summary, we conclude that the I_2O_y is unlikely to contribute to the IO_3^- signal at a significant level in atmospheric relevant conditions. Experiments carried out with ambient level precursors consistently show that gaseous I_2O_4 is significantly less abundant compared with HIO_3 (He et al., 2021b, a; Finkenzeller et al., 2022). Model simulation of iodine chemistry at the Maïdo observatory has further shown that the sum of I_2O_3 and I_2O_4 is only at around 1 % of HIO_3 thus unlikely to affect HIO_3



measurements and iodine particle formation processes in boundary layer conditions (Finkenzeller et al., 2022).

615 4 Conclusions

In this study, we present an upgraded version of the multi-scheme chemical ionisation inlet version 2 (MION2) capable of simultaneously operating atmospheric ion measurement mode and multiple chemical ionisation methods. While the concept of this inlet is identical to the MION1 (Rissanen et al., 2019), this new version improves its performance in focusing reagent ions (thus having lower LODs), enhances its operational stability and additionally allows to operate multiple chemical ionisation
620 methods with the same ionisation time.

We further developed a Python open-source flow reactor kinetic model (MARFORCE, see Shen and He (2023)) to simulate convection-diffusion-reaction equations in cylindrical flow reactors in order to calibrate gaseous species such as H_2SO_4 , HOI and HO_2 . The model is also compatible with the widely-used Master Chemical Mechanism, thus allowing future implementa-
625 tion of other chemical mechanisms.

The detection of various inorganic species using the MION2 inlet with the Br^- and NO_3^- chemical ionisation methods was further characterised at two different ionisation times. H_2SO_4 , HOI and HO_2 were calibrated by utilising the photo-chemical production in a flow reactor and quantification by the MARFORCE model. We further estimate that the LODs are around 10^5
630 molec. cm^{-3} (1-min data averaging) for e.g., H_2SO_4 and HIO_3 when the ionisation time is at 35 ms. When using a longer ionisation time (300 ms), the LOD for H_2SO_4 is further reduced to 2.9×10^4 molec. cm^{-3} (ca. 1 ppqv). A direct comparison shows that the MION2 inlet has comparable or even better LODs compared to the widely-used Eisele inlet (Jokinen et al., 2012). Therefore, the upgraded version of the inlet provides extremely high sensitivity toward measuring trace gases relevant to atmospheric particle formation.

635

Additionally, we characterised the detection of SO_2 and I_2 as they are important precursors for H_2SO_4 and HIO_3 . We found that the Br^- -MION2 is capable of detecting SO_2 by diluting a gas cylinder of a known amount of SO_2 . Besides our previous methods to calibrate gaseous I_2 (Wang et al., 2021a; Tham et al., 2021), we successfully adapted a derivatization approach in combination with high-performance liquid chromatography method which quantified iodine permeation rate of merely 17.3 ng
640 min^{-1} . The I_2 calibration of Br^- -MION2 further shows that I_2 is detected at the collision limit, similar to H_2SO_4 and consistent with our earlier estimation (Wang et al., 2021a).

As the Br^- -MION2 measures H_2O in the form of $\text{H}_2\text{O} \cdot \text{Br}^-$, we quantified the H_2O detection with a dew point mirror instrument by running them side by side. As a large portion of Br^- is converted to $\text{H}_2\text{O} \cdot \text{Br}^-$ in the ion-molecule reaction chamber,
645 we predicted the fragmentation pathways of analyte- $\text{H}_2\text{O} \cdot \text{Br}$ clusters using quantum chemical calculations. We show that H_2O



evaporates from the analyte- $\text{H}_2\text{O} \cdot \text{Br}^-$ clusters when passing the ion optics of our mass spectrometer due to the weak attachment of H_2O to the charged clusters. However, the chemical signature of the analyte is commonly preserved as the analyte- Br^- cluster or deprotonated analyte anion. Additionally, the detection using the Br^- chemical ionisation at atmospheric pressure is affected by excessive air water content. For analytes which are detected at the collision limit (e.g., H_2SO_4 , HIO_3 and I_2),
650 we find a sharp decrease in measurement sensitivity after the dew point is above 0.5 - 10.5 °C (20 - 40 % RH). The detection of weakly bonded analytes- Br^- (e.g., HO_2 and SO_2) show intensified water influence even with a dew point below 0 °C. For example, LOD of HO_2 is roughly one order of magnitude higher than H_2SO_4 at 2.7 % RH and the LOD of SO_2 is roughly three orders of magnitude higher than H_2SO_4 at below 0.1 % RH.

655 In order to reduce the detection humidity effect, a dilution method and a core-sampling method were tested in this study. We found that these methods do reduce the detection humidity effect. Both of these methods enable to detect ambient level of SO_2 (below 1 part per billion in volume) with up to 50 % RH which is otherwise not possible. It should be noted that the utilisation of these methods unavoidably dilutes the air sample thus affecting the detection of species which are less severely affected by air water content (e.g., H_2SO_4 , HOI and I_2). Therefore, these methods should be deployed only when there is a
660 clear aim, such as detecting extremely low levels of SO_2 or when the sample dew point is higher than 10 °C (40 % RH). This suggests that atmospheric pressure Br^- chemical ionisation is suitable for laboratory experiments with controlled relative humidity and ambient measurements in relatively cold environments. When interpreting data from atmospheric pressure Br^- chemical ionisation method, the impact of water should be carefully treated using analytical characterisation or fragmentation enthalpy prediction. As the MION2 allows to operate water insensitive NO_3^- chemical ionisation method and water sensitive
665 but more capable Br^- chemical ionisation method together, it will nevertheless reveal greater details of the atmosphere compared to either of these methods alone.

Finally, the measurement of gaseous HIO_3 using both the NO_3^- and Br^- chemical ionisation methods are validated. The signal of HIO_3 commonly consists of IO_3^- and either $\text{HIO}_3 \cdot \text{NO}_3^-$ or $\text{HIO}_3 \cdot \text{Br}^-$, depending on the chemical ionisation method
670 utilised. We have experimentally and theoretically validated that all of the three ions primarily originate from genuine gaseous HIO_3 and iodine oxides do not contribute to these ions at atmospherically relevant conditions.

Code availability. The MARFORCE model is shared through GitHub repository (<https://github.com/momo-catcat/MARFORCE-flowtube>). Other data analysis codes can be requested from the corresponding authors.

Data availability. Data is available upon request from the corresponding authors.



675 Appendix A

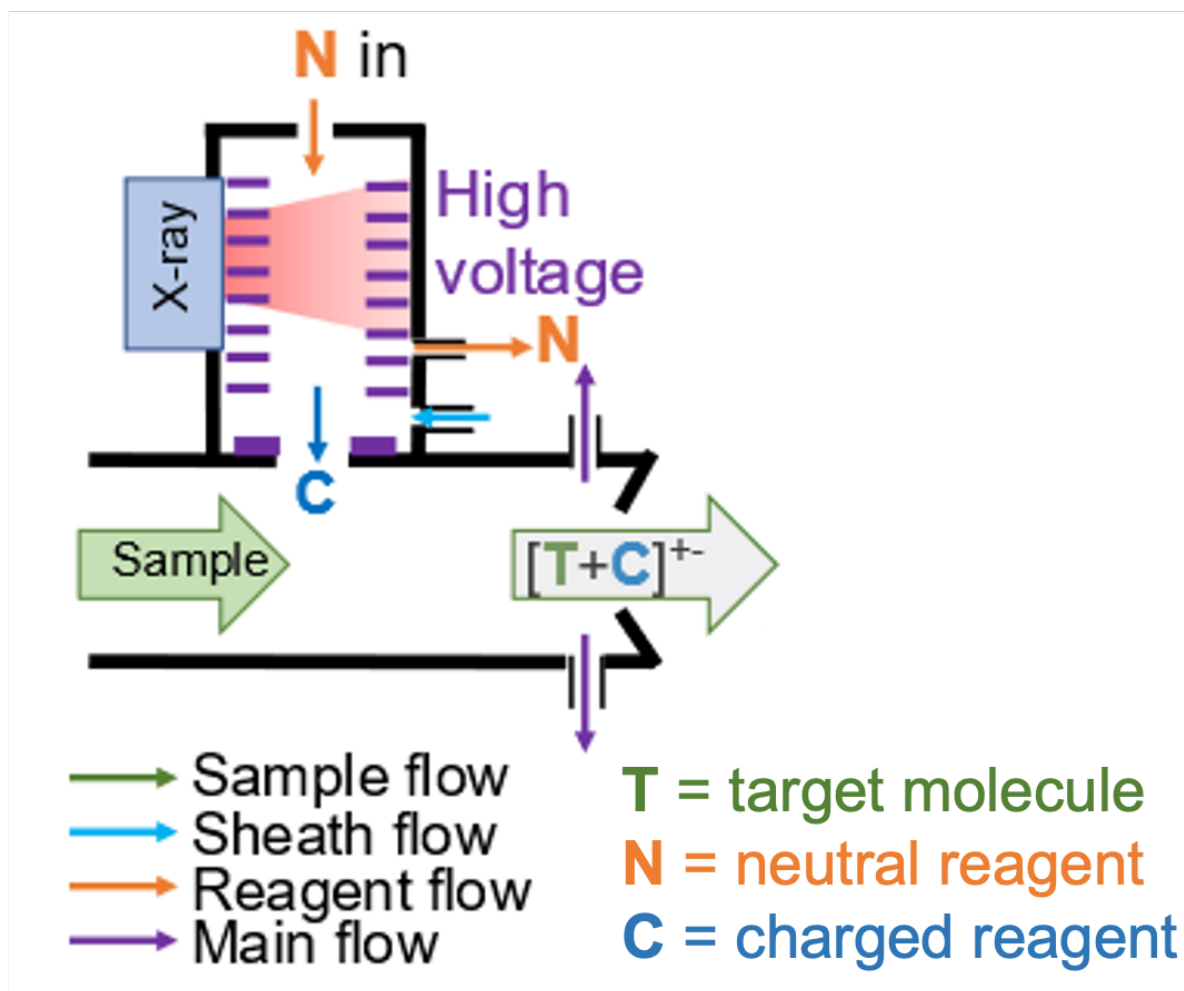


Figure A1. Schematic of the single source ionisation scheme of the MION2 inlet.

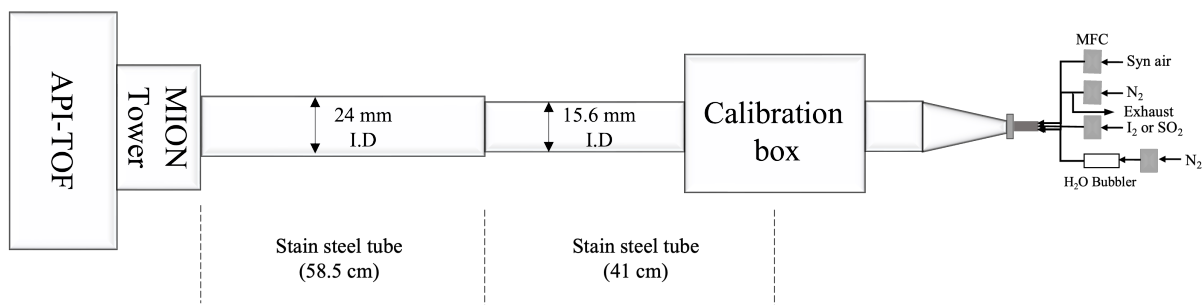


Figure A2. Schematic of a typical calibration experiment connecting the MION2 inlet (I.D. 24 mm) with the calibration source (I.D. 15.6 mm).

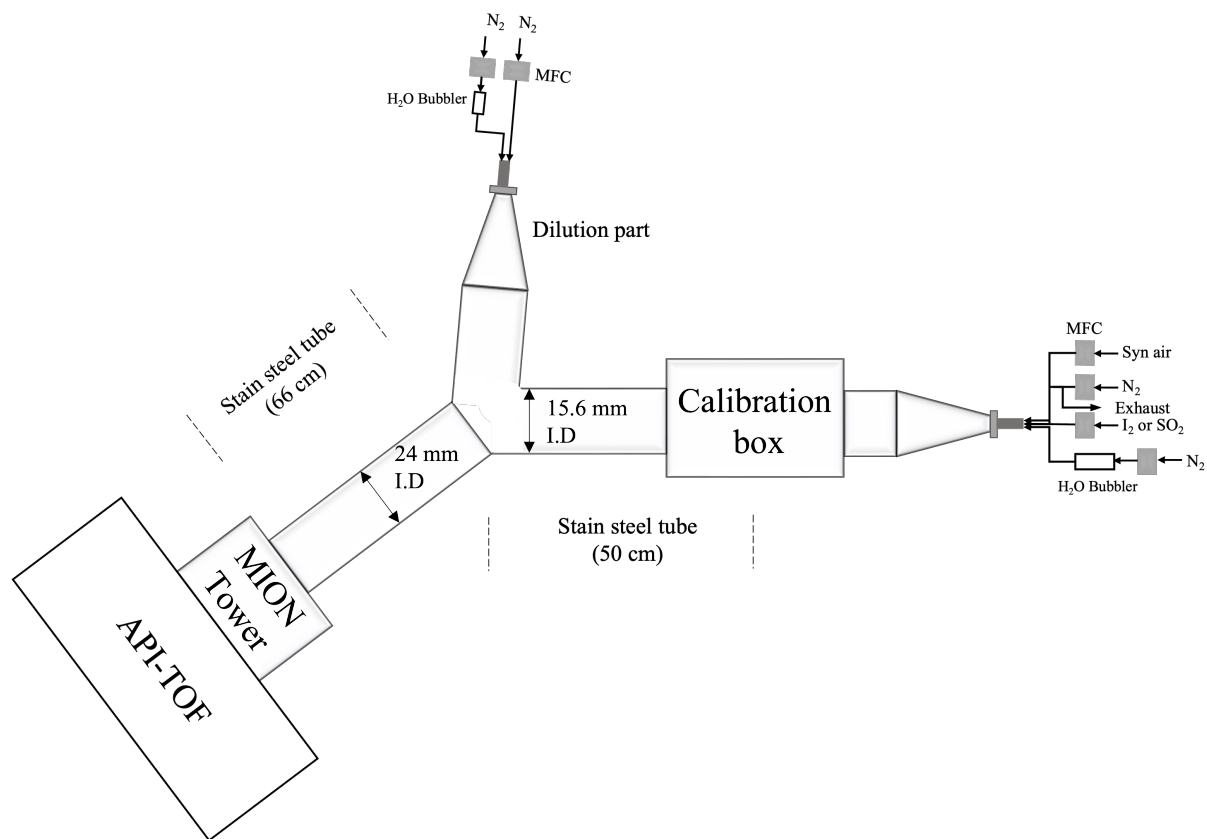


Figure A3. Schematic of the setup for examining the detection humidity effect of H_2SO_4 , HOI and HO_2 .

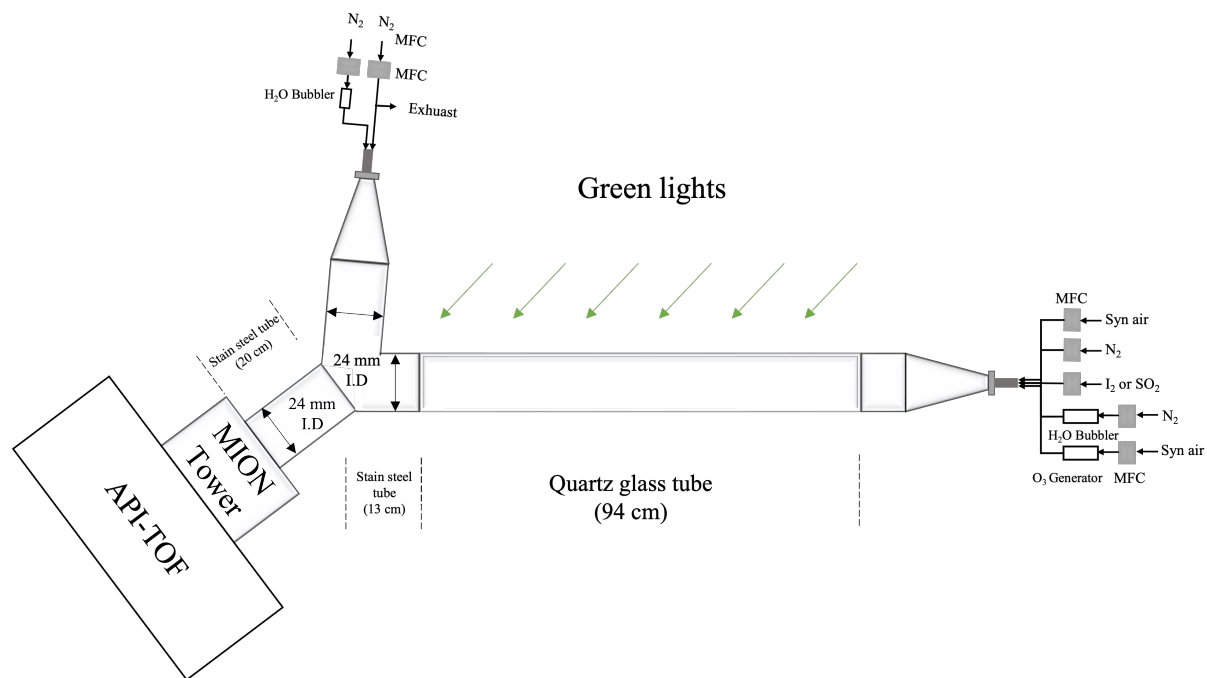


Figure A4. Schematic of the experimental setup for iodine chemistry experiments to produce higher concentrations of iodine oxides and oxoacids.

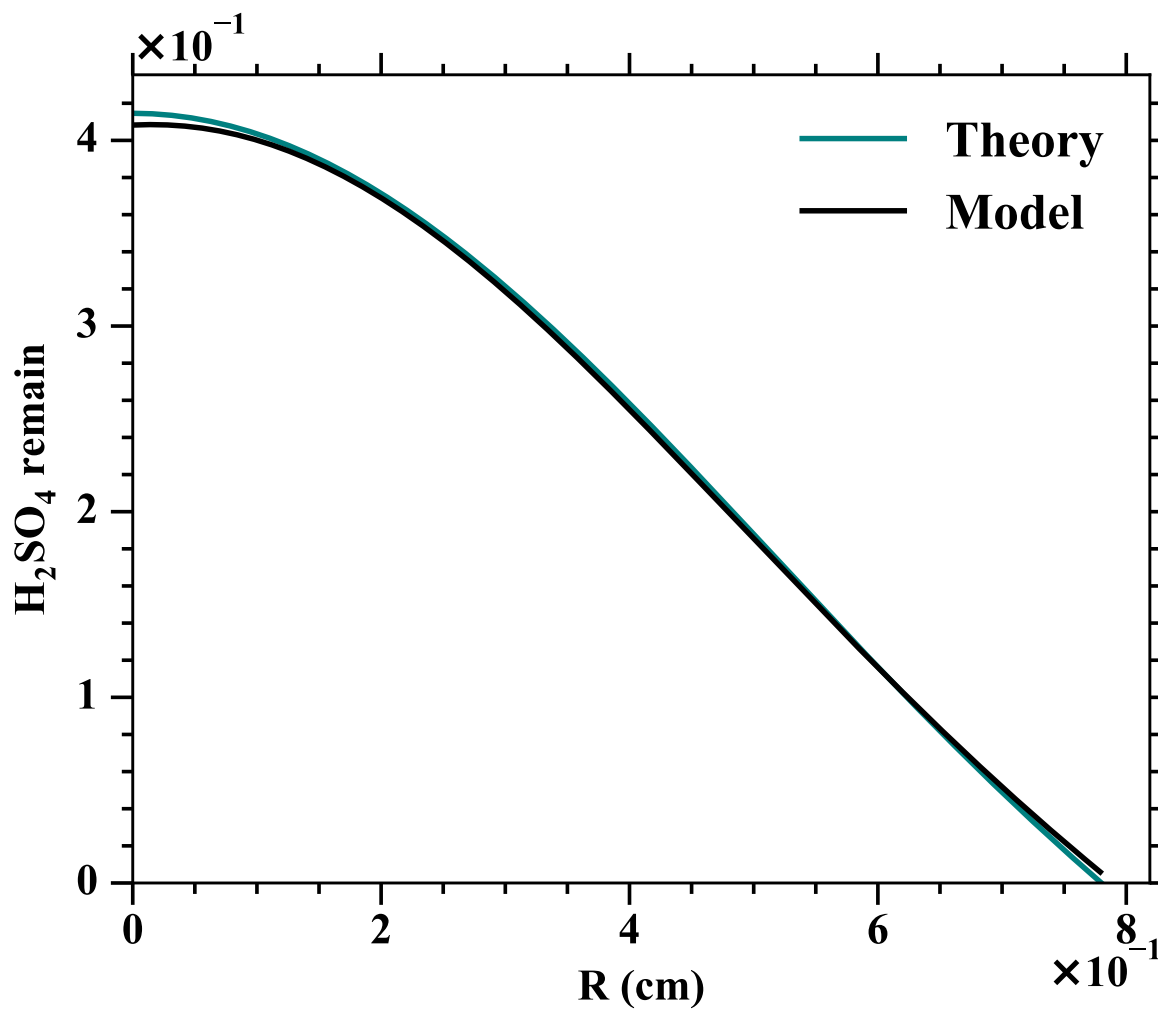


Figure A5. Comparison of the H₂SO₄ profiles at the outlet of a flow reactor. Theoretical values are predicted using Alonso et al. (2016) and the model results indicate the MARFORCE simulation. In both the theoretical prediction and the MARFORCE model, the tube length is assumed to be two meters, the inlet flow is set to 10 slpm and the diffusivity of H₂SO₄ is set to 0.088 cm²s⁻¹.

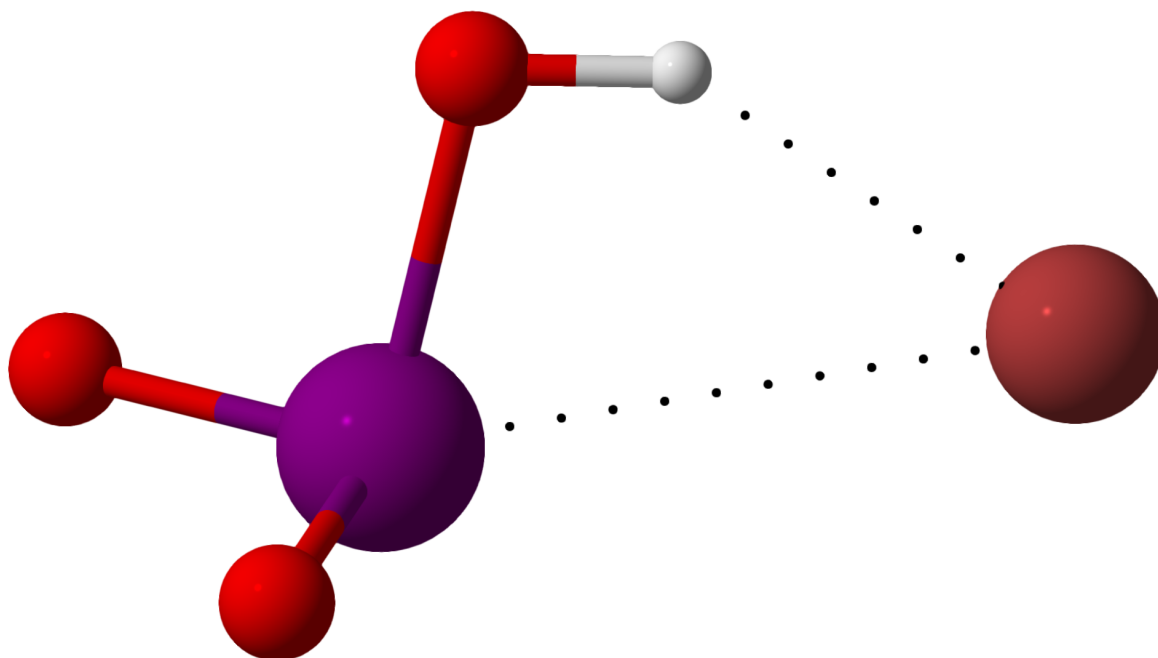


Figure A6. $\text{HIO}_3 \cdot \text{Br}^-$ geometry optimised at the $\omega\text{B97X-D/aug-cc-pVTZ-PP}$ level of theory at 298.15 K. Color coding: Iodine = purple, oxygen = red, hydrogen = white, bromine = brown.

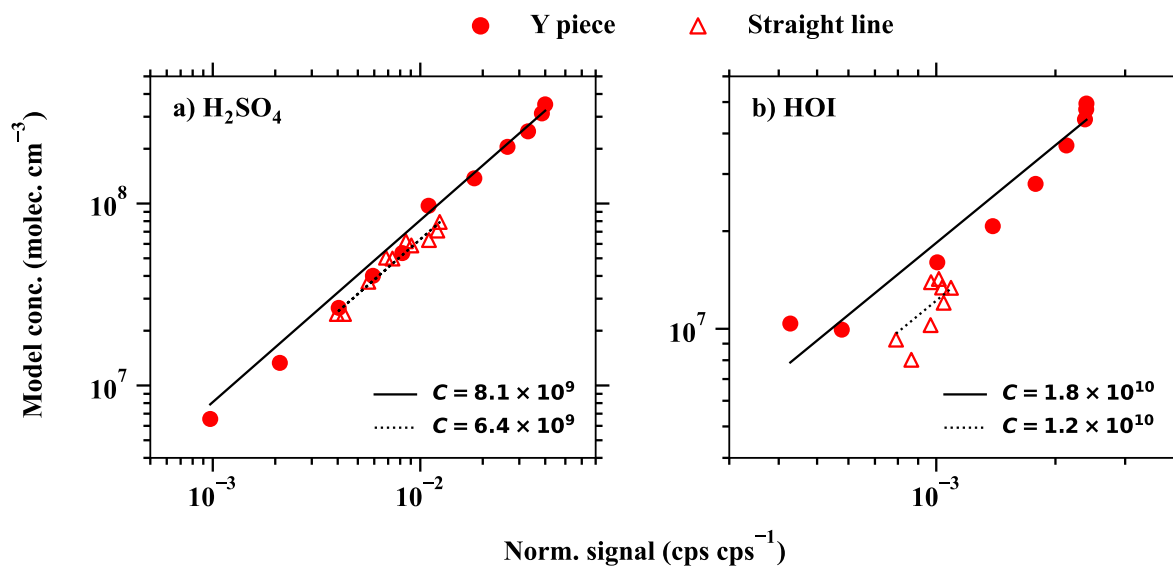


Figure A7. Comparing calibration experiments of a) H₂SO₄ and HOI with a straight tube (Figure A2) or additionally with a dilution flow (Figure A3). The difference in the calibration coefficients between the two experimental setups is the result of the less accurate representation of fluid dynamics when the dilution flow is added (Figure A3).

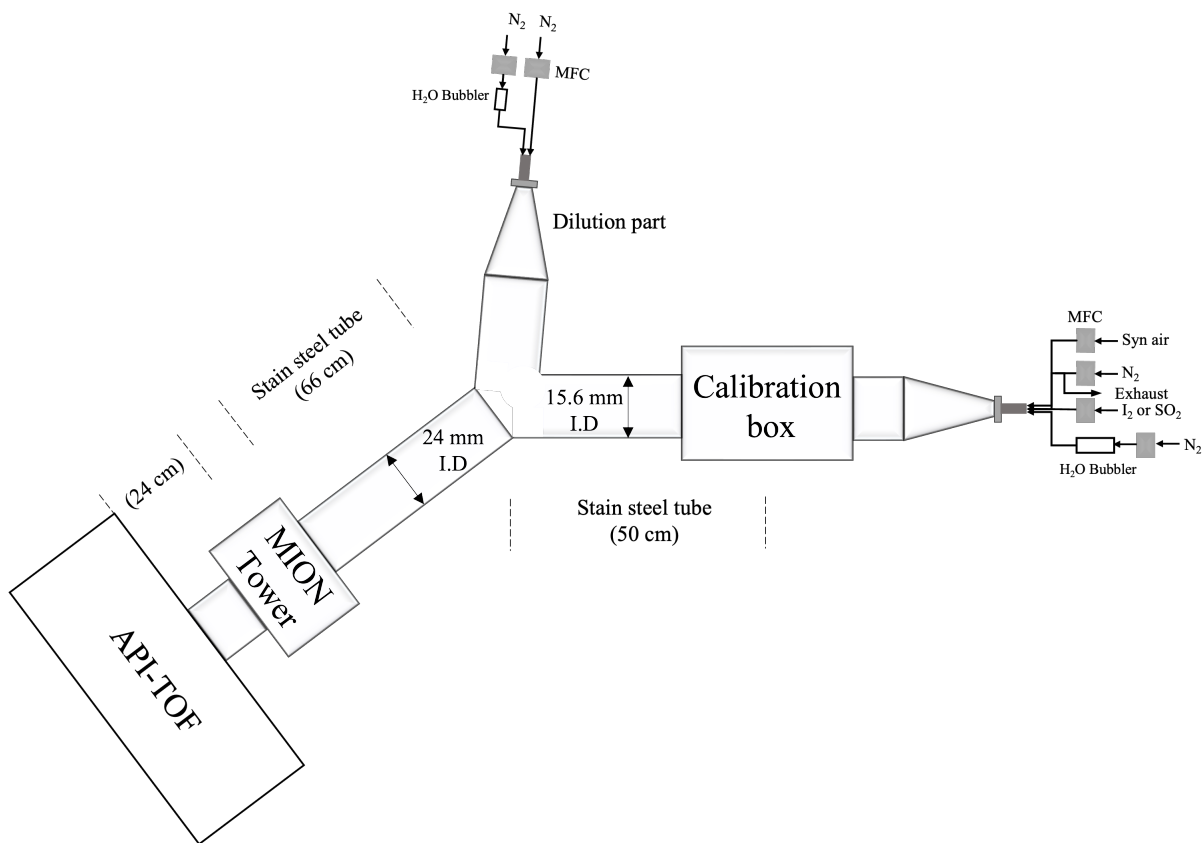


Figure A8. Schematic of the setup for H_2SO_4 , HOI and HO_2 calibration experiment with the tower 2. The difference between this setup and the one shown in Figure A3 is that the position of the MION2 tower is changed from tower 1 to tower 2.



Figure A9. The configuration of the core-sampling device (Karsa Ltd.) which is used for adjusting the sheath and sample flows.



Table A1. Chemical reactions and the reaction rate coefficients used for H₂SO₄ and HOI calibration experiments

Chemical reactions	Reaction rate coefficients
H₂SO₄ calibration:	
1. OH + SO ₂ = HSO ₃	^a $1.32 \times 10^{-12} \times (Temp/300)^{-0.7}$
2. OH + HO ₂ = H ₂ O + O ₂	^b $4.8 \times 10^{-11} \times \exp(250/Temp)$
3. HO ₂ + HO ₂ = H ₂ O ₂	^b $(2.2 \times 10^{-13} \times \exp(600/Temp) + 1.9 \times 10^{-33} \times M \times \exp(980/Temp)) \times KMT06$
4. OH + OH = H ₂ O ₂	^c $2 \times 6.9 \times 10^{-31} \times (Temp/300)^{-0.8} \times p / (1.38 \times 10^{-23}) / Temp / 10^6$
4. OH + OH = H ₂ O	^b $6.2 \times 10^{-14} \times (Temp/298)^{2.6} \times \exp(945/Temp)$
6. HSO ₃ + O ₂ = HO ₂ + SO ₃	^b $1.3 \times 10^{-12} \times \exp(-330/Temp)$
7. SO ₃ + 2H ₂ O = H ₂ SO ₄	^b $3.9 \times 10^{-41} \times \exp(6830.6/Temp)$
HOI calibration:	
1. IO + IO = I + I	^d $0.11 \times 5.4 \times 10^{-11} \times \exp(180/Temp)$
2. IO + IO = OIO + I	^d $0.38 \times 5.4 \times 10^{-11} \times \exp(180/Temp)$
3. IO + IO = I ₂ O ₂	^d $0.45 \times 5.4 \times 10^{-11} \times \exp(180/Temp)$
4. I ₂ + OH = HOI + I	^e 2.1×10^{-10}
5. IO + OIO = I ₂ O ₃	^f $w1a \times \exp(w2a \times Temp)$
6. OIO + OIO = I ₂ O ₄	^f $w1b \times \exp(w2b \times Temp)$
7. IO + OH = HO ₂ + I	^g 1.0^{-10}
8. HI + OH = H ₂ O + I	^b $1.6 \times 10^{-11} \times \exp(440/Temp)$
9. HOI + OH = H ₂ O + IO	^h 2.0×-13
10. I + HO ₂ = HI + O ₂	ⁱ $1.47 \times 10^{-11} \times \exp(-1090/Temp)$
11. IO + HO ₂ = HOI + O ₂	^b $1.4 \times 10^{-11} \times \exp(540/Temp)$
12. OH + OH = H ₂ O ₂	^c $2 \times 6.9 \times 10^{-31} \times (Temp/300)^{-0.8} \times p / (1.38 \times 10^{-23}) / Temp / 10^6$
13. OH + OH = H ₂ O	^b $6.2 \times 10^{-14} \times (Temp/298)^{2.6} \times \exp(945/Temp)$
14. OH + HO ₂ = H ₂ O + O ₂	^b $4.8 \times 10^{-11} \times \exp(250/Temp)$
15. HO ₂ + HO ₂ = H ₂ O ₂	^b $(2.2 \times 10^{-13} \times KMT06 \times \exp(600/Temp) + 1.9 \times 10^{-33} \times M \times KMT06 \times \exp(980/Temp))$

^a Wine et al. (1984); ^b Atkinson et al. (2004); ^c Zellner et al. (1988); ^d Bloss et al. (2001); ^e Gilles et al. (1999); ^f Saiz-Lopez et al. (2014); ^g Bösch (2003); ^h Chameides and Davis (1980); ⁱ Jenkin et al. (1990).

KMT06 = $1 + (1.4 \times 10^{-21} \times \exp(2200/Temp) \times [H_2O])$, [H₂O] is the absolute water concentration. *M* is the total number of molecules in the atmosphere. *p* is the pressure.

$$w1a = 4.7 \times 10^{-10} - 1.4 \times 10^{-5} \times \exp(-0.75 \times p / 1.62265) + 5.51868 \times 10^{-10} \times \exp(-0.75 \times p / 199.328);$$

$$w2a = -0.00331 - 0.00514 \times \exp(-0.75 \times p / 325.68711) - 0.00444 \times \exp(-0.75 \times p / 40.81609);$$

$$w1b = 1.166 \times 10^{-9} - 7.796 \times 10^{-10} \times \exp(-0.75 \times p / 22.093) + 1.038 \times 10^{-9} \times \exp(-0.75 \times p / 568.154);$$

$$w2b = -0.00813 - 0.00382 \times \exp(-0.75 \times p / 45.57591) - 0.00643 \times \exp(-0.75 \times p / 417.95061).$$



Author contributions. X.-C.H. and J.S. designed and carried out the experiments. J.S. and X.-C.H. wrote the MARFORCE model. J.Z. wrote the documentation of the MARFORCE model. S.I. carried out quantum chemical calculations. N.M.M., M.Koi. and M.M.K. analysed molecular iodine samples. J.K., P.J., M.S. and J.M. provided technical support. X.-C.H. wrote the manuscript with contributions from J.S., N.M.M., P.J. and S.I. Finally, J.K., J.S., M.R., S.I., D.R.W. and M.Kul. commented on and edited the manuscript.

680 *Competing interests.* Paxton Juuti and Jyri Mikkilä work for Karsa, Ltd. Finland. Juha Kangasluoma works partially for Karsa, Ltd. Finland

Acknowledgements. We thank the ACCC Flagship funded by the Academy of Finland grant number 337549, the Academy professorship funded by the Academy of Finland (grant no. 302958), Academy of Finland projects no. 331207, 346370, 325656, 316114, 314798, 325647, 341349 and 349659. This project has received funding from the European Research Council under the European Union's Horizon 2020 research and innovation programme under Grant Contract No. 742206 and 101002728. The Arena for the gap analysis of the existing
685 Arctic Science Co-Operations (AASCO) funded by Prince Albert Foundation Contract No 2859. M.Kul. thanks the Jane and Aatos Erkkö Foundation for providing funding. M.Kul. and X.-C.H thank the Jenny and Antti Wihuri Foundation for funding this research. We also thank Miska Olin, Gustaf Lönn and Heikki Junninen for their helpful discussions and contributions to the MARFORCE model. Simon Patrick O'Meara and Gordon McFiggans are acknowledged for their contributions to the MCM interpreter in the MARFORCE model.



References

- 690 Agarwal, B., González-Méndez, R., Lanza, M., Sulzer, P., Märk, T. D., Thomas, N., and Mayhew, C. A.: Sensitivity and Selectivity of Switchable Reagent Ion Soft Chemical Ionization Mass Spectrometry for the Detection of Picric Acid, *The Journal of Physical Chemistry A*, 118, 8229–8236, <https://doi.org/10.1021/jp5010192>, 2014.
- Alonso, M., Carsí, M., and Huang, C.-H.: Using the fully developed concentration profile to determine particle penetration in a laminar flow tube, *Journal of Aerosol Science*, 97, 34–37, <https://doi.org/10.1016/j.jaerosci.2016.04.002>, 2016.
- 695 Atkinson, R., Baulch, D. L., Cox, R. A., Crowley, J. N., Hampson, R. F., Hynes, R. G., Jenkin, M. E., Rossi, M. J., and Troe, J.: Evaluated kinetic and photochemical data for atmospheric chemistry: Volume I - gas phase reactions of O_x, HO_x, NO_x and SO_x species, *Atmospheric Chemistry and Physics*, 4, 1461–1738, <https://doi.org/10.5194/acp-4-1461-2004>, 2004.
- Baccarini, A., Karlsson, L., Dommen, J., Duplessis, P., Vüllers, J., Brooks, I. M., Saiz-Lopez, A., Salter, M., Tjernström, M., Baltensperger, U., Zieger, P., and Schmale, J.: Frequent new particle formation over the high Arctic pack ice by enhanced iodine emissions, *Nature*
- 700 *Communications*, 11, 4924, <https://doi.org/10.1038/s41467-020-18551-0>, 2020.
- Berndt, T., Richters, S., Jokinen, T., Hyttinen, N., Kurtén, T., Otkjær, R. V., Kjaergaard, H. G., Stratmann, F., Herrmann, H., Sipilä, M., Kulmala, M., and Ehn, M.: Hydroxyl radical-induced formation of highly oxidized organic compounds, *Nature Communications*, 7, 13 677, <https://doi.org/10.1038/ncomms13677>, 2016.
- Bloss, W. J., Rowley, D. M., Cox, R. A., and Jones, R. L.: Kinetics and Products of the IO Self-Reaction, *The Journal of Physical Chemistry*
- 705 *A*, 105, 7840–7854, <https://doi.org/10.1021/jp0044936>, 2001.
- Breitenlechner, M., Fischer, L., Hainer, M., Heinritzi, M., Curtius, J., and Hansel, A.: PTR3: An Instrument for Studying the Lifecycle of Reactive Organic Carbon in the Atmosphere, *Analytical Chemistry*, 89, 5824–5831, <https://doi.org/10.1021/acs.analchem.6b05110>, 2017.
- Brophy, P. and Farmer, D. K.: A switchable reagent ion high resolution time-of-flight chemical ionization mass spectrometer for real-time measurement of gas phase oxidized species: characterization from the 2013 southern oxidant and aerosol study, *Atmospheric Measurement*
- 710 *Techniques*, 8, 2945–2959, <https://doi.org/10.5194/amt-8-2945-2015>, 2015.
- Bösch, H.: Upper limits of stratospheric IO and OIO inferred from center-to-limb-darkening-corrected balloon-borne solar occultation visible spectra: Implications for total gaseous iodine and stratospheric ozone, *Journal of Geophysical Research*, 108, 4455, <https://doi.org/10.1029/2002JD003078>, 2003.
- Caldwell, G. W., Masucci, J. A., and Ikonou, M. G.: Negative ion chemical ionization mass spectrometry—binding of molecules to bromide and iodide anions, *Organic Mass Spectrometry*, 24, 8–14, <https://doi.org/10.1002/oms.1210240103>, 1989.
- Chai, J.-D. and Head-Gordon, M.: Long-range corrected hybrid density functionals with damped atom–atom dispersion corrections, *Physical Chemistry Chemical Physics*, 10, 6615, <https://doi.org/10.1039/b810189b>, 2008.
- Chameides, W. L. and Davis, D. D.: Iodine: Its possible role in tropospheric photochemistry, *Journal of Geophysical Research: Oceans*, 85, 7383–7398, <https://doi.org/10.1029/JC085iC12p07383>, 1980.
- 720 Creasey, D. J., Heard, D. E., and Lee, J. D.: Absorption cross-section measurements of water vapour and oxygen at 185 nm. Implications for the calibration of field instruments to measure OH, HO₂ and RO₂ radicals, *Geophysical Research Letters*, 27, 1651–1654, <https://doi.org/10.1029/1999GL011014>, 2000.
- Ehn, M., Thornton, J. A., Kleist, E., Sipilä, M., Junninen, H., Pullinen, I., Springer, M., Rubach, F., Tillmann, R., Lee, B., Lopez-Hilfiker, F., Andres, S., Acir, I.-H., Rissanen, M., Jokinen, T., Schobesberger, S., Kangasluoma, J., Kontkanen, J., Nieminen, T., Kurtén, T., Nielsen, L. B., Jørgensen, S., Kjaergaard, H. G., Canagaratna, M., Maso, M. D., Berndt, T., Petäjä, T., Wahner, A., Kerminen, V.-M., Kulmala,
- 725



- M., Worsnop, D. R., Wildt, J., and Mentel, T. F.: A large source of low-volatility secondary organic aerosol, *Nature*, 506, 476–479, <https://doi.org/10.1038/nature13032>, 2014.
- Eisele, F. L. and Tanner, D. J.: Measurement of the gas phase concentration of H₂SO₄ and methane sulfonic acid and estimates of H₂SO₄ production and loss in the atmosphere, *Journal of Geophysical Research: Atmospheres*, 98, 9001–9010, <https://doi.org/10.1029/93JD00031>, 1993.
- Feller, D.: The role of databases in support of computational chemistry calculations, *Journal of Computational Chemistry*, 17, 1571–1586, [https://doi.org/10.1002/\(SICI\)1096-987X\(199610\)17:13<1571::AID-JCC9>3.0.CO;2-P](https://doi.org/10.1002/(SICI)1096-987X(199610)17:13<1571::AID-JCC9>3.0.CO;2-P), 1996.
- Finkenzeller, H., Iyer, S., He, X.-C., Simon, M., Koenig, T. K., Lee, C. F., Valiev, R., Hofbauer, V., Amorim, A., Baalbaki, R., Baccharini, A., Beck, L., Bell, D. M., Caudillo, L., Chen, D., Chiu, R., Chu, B., Dada, L., Duplissy, J., Heinritzi, M., Kempainen, D., Kim, C., Krechmer, J., Kürten, A., Kvashnin, A., Lamkaddam, H., Lee, C. P., Lehtipalo, K., Li, Z., Makhmutov, V., Manninen, H. E., Marie, G., Marten, R., Mauldin, R. L., Mentler, B., Müller, T., Petäjä, T., Philippov, M., Ranjithkumar, A., Rörup, B., Shen, J., Stolzenburg, D., Tauber, C., Tham, Y. J., Tomé, A., Vazquez-Pufleau, M., Wagner, A. C., Wang, D. S., Wang, M., Wang, Y., Weber, S. K., Nie, W., Wu, Y., Xiao, M., Ye, Q., Zauner-Wieczorek, M., Hansel, A., Baltensperger, U., Brioude, J., Curtius, J., Donahue, N. M., Haddad, I. E., Flagan, R. C., Kulmala, M., Kirkby, J., Sipilä, M., Worsnop, D. R., Kurten, T., Rissanen, M., and Volkamer, R.: The gas-phase formation mechanism of iodic acid as an atmospheric aerosol source, *Nature Chemistry*, <https://doi.org/10.1038/s41557-022-01067-z>, 2022.
- Frisch, M. J., Trucks, G. W., Schlegel, H. B., Scuseria, G. E., Robb, M. A., Cheeseman, J. R., Scalmani, G., Barone, V., Petersson, G. A., Nakatsuji, H., Li, X., Caricato, M., Marenich, A. V., Bloino, J., Janesko, B. G., Gomperts, R., Mennucci, B., Hratchian, H. P., Ortiz, J. V., Izmaylov, A. F., Sonnenberg, J. L., Williams, Ding, F., Lipparini, F., Egidi, F., Goings, J., Peng, B., Petrone, A., Henderson, T., Ranasinghe, D., Zakrzewski, V. G., Gao, J., Rega, N., Zheng, G., Liang, W., Hada, M., Ehara, M., Toyota, K., Fukuda, R., Hasegawa, J., Ishida, M., Nakajima, T., Honda, Y., Kitao, O., Nakai, H., Vreven, T., Throssell, K., Montgomery Jr., J. A., Peralta, J. E., Ogliaro, F., Bearpark, M. J., Heyd, J. J., Brothers, E. N., Kudin, K. N., Staroverov, V. N., Keith, T. A., Kobayashi, R., Normand, J., Raghavachari, K., Rendell, A. P., Burant, J. C., Iyengar, S. S., Tomasi, J., Cossi, M., Millam, J. M., Klene, M., Adamo, C., Cammi, R., Ochterski, J. W., Martin, R. L., Morokuma, K., Farkas, O., Foresman, J. B., and Fox, D. J.: Gaussian 16 Rev. C.01, 2016.
- Fuller, E. N., Schettler, P. D., and Giddings, J. C.: NEW METHOD FOR PREDICTION OF BINARY GAS-PHASE DIFFUSION COEFFICIENTS, *Industrial & Engineering Chemistry*, 58, 18–27, <https://doi.org/10.1021/ie50677a007>, 1966.
- Gilles, M. K., Burkholder, J. B., and Ravishankara, A. R.: Rate coefficients for the reaction of OH with Cl₂, Br₂, and I₂ from 235 to 354 K, *International Journal of Chemical Kinetics*, 31, 417–424, [https://doi.org/10.1002/\(SICI\)1097-4601\(1999\)31:6<417::AID-KIN3>3.0.CO;2-A](https://doi.org/10.1002/(SICI)1097-4601(1999)31:6<417::AID-KIN3>3.0.CO;2-A), 1999.
- Gormley, P. and Kennedy, M.: Diffusion from a stream flowing through a cylindrical tube, in: *Proceedings of the Royal Irish Academy. Section A: Mathematical and Physical Sciences*, vol. 52, pp. 163–169, JSTOR, 1948.
- Gálvez, O., Gómez Martín, J. C., Gómez, P. C., Saiz-Lopez, A., and Pacios, L. F.: A theoretical study on the formation of iodine oxide aggregates and monohydrates, *Physical Chemistry Chemical Physics*, 15, 15 572, <https://doi.org/10.1039/c3cp51219c>, 2013.
- Gómez Martín, J. C., Lewis, T. R., Blitz, M. A., Plane, J. M. C., Kumar, M., Francisco, J. S., and Saiz-Lopez, A.: A gas-to-particle conversion mechanism helps to explain atmospheric particle formation through clustering of iodine oxides, *Nature Communications*, 11, 4521, <https://doi.org/10.1038/s41467-020-18252-8>, 2020.
- Gómez Martín, J. C., Lewis, T. R., James, A. D., Saiz-Lopez, A., and Plane, J. M. C.: Insights into the Chemistry of Iodine New Particle Formation: The Role of Iodine Oxides and the Source of Iodic Acid, *Journal of the American Chemical Society*, p. jacs.1c12957, <https://doi.org/10.1021/jacs.1c12957>, 2022.



- Hansel, A., Jordan, A., Holzinger, R., Prazeller, P., Vogel, W., and Lindinger, W.: Proton transfer reaction mass spectrometry: on-line trace gas analysis at the ppb level, *International Journal of Mass Spectrometry and Ion Processes*, 149–150, 609–619, [https://doi.org/10.1016/0168-1176\(95\)04294-U](https://doi.org/10.1016/0168-1176(95)04294-U), 1995.
- Hanson, D. R. and Eisele, F.: Diffusion of H₂SO₄ in Humidified Nitrogen: Hydrated H₂SO₄, *The Journal of Physical Chemistry A*, 104, 1715–1719, <https://doi.org/10.1021/jp993622j>, 2000.
- He, X.-C.: From the measurement of halogenated species to iodine particle formation, Ph.D. thesis, University of Helsinki, Helsinki, <https://helda.helsinki.fi/handle/10138/229173>, 2017.
- He, X.-C., Iyer, S., Sipilä, M., Ylisirniö, A., Peltola, M., Kontkanen, J., Baalbaki, R., Simon, M., Kürten, A., Tham, Y. J., Pesonen, J., Ahonen, L. R., Amanatidis, S., Amorim, A., Baccarini, A., Beck, L., Bianchi, F., Brilke, S., Chen, D., Chiu, R., Curtius, J., Dada, L., Dias, A., Dommen, J., Donahue, N. M., Duplissy, J., El Haddad, I., Finkenzeller, H., Fischer, L., Heinritzi, M., Hofbauer, V., Kangasluoma, J., Kim, C., Koenig, T. K., Kubečka, J., Kvashnin, A., Lamkaddam, H., Lee, C. P., Leiminger, M., Li, Z., Makhmutov, V., Xiao, M., Marten, R., Nie, W., Onnela, A., Partoll, E., Petäjä, T., Salo, V.-T., Schuchmann, S., Steiner, G., Stolzenburg, D., Stozhkov, Y., Tauber, C., Tomé, A., Väisänen, O., Vazquez-Pufleau, M., Volkamer, R., Wagner, A. C., Wang, M., Wang, Y., Wimmer, D., Winkler, P. M., Worsnop, D. R., Wu, Y., Yan, C., Ye, Q., Lehtinen, K., Nieminen, T., Manninen, H. E., Rissanen, M., Schobesberger, S., Lehtipalo, K., Baltensperger, U., Hansel, A., Kerminen, V.-M., Flagan, R. C., Kirkby, J., Kurtén, T., and Kulmala, M.: Determination of the collision rate coefficient between charged iodic acid clusters and iodic acid using the appearance time method, *Aerosol Science and Technology*, 55, 231–242, <https://doi.org/10.1080/02786826.2020.1839013>, 2021a.
- He, X.-C., Tham, Y. J., Dada, L., Wang, M., Finkenzeller, H., Stolzenburg, D., Iyer, S., Simon, M., Kürten, A., Shen, J., Rörup, B., Rissanen, M., Schobesberger, S., Baalbaki, R., Wang, D. S., Koenig, T. K., Jokinen, T., Sarnela, N., Beck, L. J., Almeida, J., Amanatidis, S., Amorim, A., Ataei, F., Baccarini, A., Bertozzi, B., Bianchi, F., Brilke, S., Caudillo, L., Chen, D., Chiu, R., Chu, B., Dias, A., Ding, A., Dommen, J., Duplissy, J., El Haddad, I., Gonzalez Carracedo, L., Granzin, M., Hansel, A., Heinritzi, M., Hofbauer, V., Junninen, H., Kangasluoma, J., Kemppainen, D., Kim, C., Kong, W., Krechmer, J. E., Kvashin, A., Laitinen, T., Lamkaddam, H., Lee, C. P., Lehtipalo, K., Leiminger, M., Li, Z., Makhmutov, V., Manninen, H. E., Marie, G., Marten, R., Mathot, S., Mauldin, R. L., Mentler, B., Möhler, O., Müller, T., Nie, W., Onnela, A., Petäjä, T., Pfeifer, J., Philippov, M., Ranjithkumar, A., Saiz-Lopez, A., Salma, I., Scholz, W., Schuchmann, S., Schulze, B., Steiner, G., Stozhkov, Y., Tauber, C., Tomé, A., Thakur, R. C., Väisänen, O., Vazquez-Pufleau, M., Wagner, A. C., Wang, Y., Weber, S. K., Winkler, P. M., Wu, Y., Xiao, M., Yan, C., Ye, Q., Ylisirniö, A., Zauner-Wieczorek, M., Zha, Q., Zhou, P., Flagan, R. C., Curtius, J., Baltensperger, U., Kulmala, M., Kerminen, V.-M., Kurtén, T., Donahue, N. M., Volkamer, R., Kirkby, J., Worsnop, D. R., and Sipilä, M.: Role of iodine oxoacids in atmospheric aerosol nucleation, *Science*, 371, 589–595, <https://doi.org/10.1126/science.abe0298>, 2021b.
- Hearn, J. D. and Smith, G. D.: A Chemical Ionization Mass Spectrometry Method for the Online Analysis of Organic Aerosols, *Analytical Chemistry*, 76, 2820–2826, <https://doi.org/10.1021/ac049948s>, 2004.
- Hoffmann, T., O'Dowd, C. D., and Seinfeld, J. H.: Iodine oxide homogeneous nucleation: An explanation for coastal new particle production, *Geophysical Research Letters*, 28, 1949–1952, <https://doi.org/10.1029/2000GL012399>, 2001.
- Huey, L. G.: Measurement of trace atmospheric species by chemical ionization mass spectrometry: Speciation of reactive nitrogen and future directions, *Mass Spectrometry Reviews*, 26, 166–184, <https://doi.org/10.1002/mas.20118>, 2007.
- Iyer, S., Lopez-Hilfiker, F., Lee, B. H., Thornton, J. A., and Kurtén, T.: Modeling the Detection of Organic and Inorganic Compounds Using Iodide-Based Chemical Ionization, *The Journal of Physical Chemistry A*, 120, 576–587, <https://doi.org/10.1021/acs.jpca.5b09837>, 2016.



- 800 Iyer, S., He, X., Hyttinen, N., Kurtén, T., and Rissanen, M. P.: Computational and Experimental Investigation of the Detection of HO₂ Radical and the Products of Its Reaction with Cyclohexene Ozonolysis Derived RO₂ Radicals by an Iodide-Based Chemical Ionization Mass Spectrometer, *The Journal of Physical Chemistry A*, 121, 6778–6789, <https://doi.org/10.1021/acs.jpca.7b01588>, 2017.
- Jenkin, M. E., Cox, R. A., Mellouki, A., Le Bras, G., and Poulet, G.: Kinetics of the reaction of iodine atoms with hydroperoxy radicals, *The Journal of Physical Chemistry*, 94, 2927–2934, <https://doi.org/10.1021/j100370a036>, 1990.
- 805 Jenkin, M. E., Saunders, S. M., and Pilling, M. J.: The tropospheric degradation of volatile organic compounds: a protocol for mechanism development, *Atmospheric Environment*, 31, 81–104, [https://doi.org/10.1016/S1352-2310\(96\)00105-7](https://doi.org/10.1016/S1352-2310(96)00105-7), 1997.
- Jokinen, T., Sipilä, M., Junninen, H., Ehn, M., Lönn, G., Hakala, J., Petäjä, T., Mauldin, R. L., Kulmala, M., and Worsnop, D. R.: Atmospheric sulphuric acid and neutral cluster measurements using CI-API-TOF, *Atmospheric Chemistry and Physics*, 12, 4117–4125, <https://doi.org/10.5194/acp-12-4117-2012>, 2012.
- 810 Jordan, A., Haidacher, S., Hanel, G., Hartungen, E., Herbig, J., Märk, L., Schottkowsky, R., Seehauser, H., Sulzer, P., and Märk, T.: An online ultra-high sensitivity Proton-transfer-reaction mass-spectrometer combined with switchable reagent ion capability (PTR+SRI-MS), *International Journal of Mass Spectrometry*, 286, 32–38, <https://doi.org/10.1016/j.ijms.2009.06.006>, 2009.
- Junninen, H., Ehn, M., Petäjä, T., Luosujärvi, L., Kotiaho, T., Kostianen, R., Rohner, U., Gonin, M., Fuhrer, K., Kulmala, M., and Worsnop, D. R.: A high-resolution mass spectrometer to measure atmospheric ion composition, *Atmospheric Measurement Techniques*, 3, 1039–1053, <https://doi.org/10.5194/amt-3-1039-2010>, 2010.
- 815 Kendall, R. A., Dunning, T. H., and Harrison, R. J.: Electron affinities of the first-row atoms revisited. Systematic basis sets and wave functions, *The Journal of Chemical Physics*, 96, 6796–6806, <https://doi.org/10.1063/1.462569>, 1992.
- Kercher, J. P., Riedel, T. P., and Thornton, J. A.: Chlorine activation by N₂O₅: simultaneous, in situ detection of ClNO₂ and N₂O₅ by chemical ionization mass spectrometry, *Atmos. Meas. Tech.*, 2, 193–204, <https://doi.org/10.5194/amt-2-193-2009>, 2009.
- 820 Kirkby, J., Curtius, J., Almeida, J., Dunne, E., Duplissy, J., Ehrhart, S., Franchin, A., Gagné, S., Ickes, L., Kürten, A., Kupc, A., Metzger, A., Riccobono, F., Rondo, L., Schobesberger, S., Tsagkogeorgas, G., Wimmer, D., Amorim, A., Bianchi, F., Breitenlechner, M., David, A., Dommen, J., Downard, A., Ehn, M., Flagan, R. C., Haider, S., Hansel, A., Hauser, D., Jud, W., Junninen, H., Kreissl, F., Kvashin, A., Laaksonen, A., Lehtipalo, K., Lima, J., Lovejoy, E. R., Makhmutov, V., Mathot, S., Mikkilä, J., Minginette, P., Mogo, S., Nieminen, T., Onnela, A., Pereira, P., Petäjä, T., Schnitzhofer, R., Seinfeld, J. H., Sipilä, M., Stozhkov, Y., Stratmann, F., Tomé, A., Vanhanen, J., Viisanen, Y., Vrtala, A., Wagner, P. E., Walther, H., Weingartner, E., Wex, H., Winkler, P. M., Carslaw, K. S., Worsnop, D. R., Baltensperger, U., and Kulmala, M.: Role of sulphuric acid, ammonia and galactic cosmic rays in atmospheric aerosol nucleation, *Nature*, 476, 429–433, <https://doi.org/10.1038/nature10343>, 2011.
- Kürten, A., Rondo, L., Ehrhart, S., and Curtius, J.: Calibration of a Chemical Ionization Mass Spectrometer for the Measurement of Gaseous Sulfuric Acid, *The Journal of Physical Chemistry A*, 116, 6375–6386, <https://doi.org/10.1021/jp212123n>, 2012.
- 830 Lagg, A., Taucher, J., Hansel, A., and Lindinger, W.: Applications of proton transfer reactions to gas analysis, *International Journal of Mass Spectrometry and Ion Processes*, 134, 55–66, [https://doi.org/10.1016/0168-1176\(94\)03965-8](https://doi.org/10.1016/0168-1176(94)03965-8), 1994.
- Laskin, J., Laskin, A., and Nizkorodov, S. A.: Mass Spectrometry Analysis in Atmospheric Chemistry, *Analytical Chemistry*, 90, 166–189, <https://doi.org/10.1021/acs.analchem.7b04249>, 2018.
- 835 Lee, B. H., Lopez-Hilfiker, F. D., Mohr, C., Kurtén, T., Worsnop, D. R., and Thornton, J. A.: An Iodide-Adduct High-Resolution Time-of-Flight Chemical-Ionization Mass Spectrometer: Application to Atmospheric Inorganic and Organic Compounds, *Environmental Science & Technology*, 48, 6309–6317, <https://doi.org/10.1021/es500362a>, 2014.



- Liao, J., Huey, L. G., Liu, Z., Tanner, D. J., Cantrell, C. A., Orlando, J. J., Flocke, F. M., Shepson, P. B., Weinheimer, A. J., Hall, S. R., Ullmann, K., Beine, H. J., Wang, Y., Ingall, E. D., Stephens, C. R., Hornbrook, R. S., Apel, E. C., Riemer, D., Fried, A., Mauldin, R. L., Smith, J. N., Staebler, R. M., Neuman, J. A., and Nowak, J. B.: High levels of molecular chlorine in the Arctic atmosphere, *Nature Geoscience*, 7, 91–94, <https://doi.org/10.1038/ngeo2046>, 2014.
- 840 Liu, L., Li, S., Zu, H., and Zhang, X.: Unexpectedly significant stabilizing mechanism of iodic acid on iodine acid nucleation under different atmospheric conditions, *Science of The Total Environment*, 859, 159–172, <https://doi.org/10.1016/j.scitotenv.2022.159832>, 2023.
- Lopez-Hilfiker, F. D., Iyer, S., Mohr, C., Lee, B. H., D'Ambro, E. L., Kurtén, T., and Thornton, J. A.: Constraining the sensitivity of iodide adduct chemical ionization mass spectrometry to multifunctional organic molecules using the collision limit and thermodynamic stability of iodide ion adducts, *Atmospheric Measurement Techniques*, 9, 1505–1512, <https://doi.org/10.5194/amt-9-1505-2016>, 2016.
- 845 Mielke, L. H., Furgeson, A., and Osthoff, H. D.: Observation of ClNO₂ in a Mid-Continental Urban Environment, *Environmental Science & Technology*, 45, 8889–8896, <https://doi.org/10.1021/es201955u>, 2011.
- Mishra, S., Singh, V., Jain, A., and Verma, K. K.: Determination of iodide by derivatization to 4-iodo-N,N-dimethylaniline and gas chromatography–mass spectrometry, *The Analyst*, 125, 459–464, <https://doi.org/10.1039/a908363d>, 2000.
- 850 Munson, M. S. B. and Field, F. H.: Chemical Ionization Mass Spectrometry. I. General Introduction, *Journal of the American Chemical Society*, 88, 2621–2630, <https://doi.org/10.1021/ja00964a001>, 1966.
- Neese, F.: The ORCA program system: The ORCA program system, *Wiley Interdisciplinary Reviews: Computational Molecular Science*, 2, 73–78, <https://doi.org/10.1002/wcms.81>, 2012.
- O'Dowd, C. D., Jimenez, J. L., Bahreini, R., Flagan, R. C., Seinfeld, J. H., Hämeri, K., Pirjola, L., Kulmala, M., Jennings, S. G., and Hoffmann, T.: Marine aerosol formation from biogenic iodine emissions, *Nature*, 417, 632–636, <https://doi.org/10.1038/nature00775>, 2002.
- 855 O'Meara, S. P., Xu, S., Topping, D., Alfarra, M. R., Capes, G., Lowe, D., Shao, Y., and McFiggans, G.: PyCHAM (v2.1.1): a Python box model for simulating aerosol chambers, *Geoscientific Model Development*, 14, 675–702, <https://doi.org/10.5194/gmd-14-675-2021>, 2021.
- Pan, Y., Zhang, Q., Zhou, W., Zou, X., Wang, H., Huang, C., Shen, C., and Chu, Y.: Detection of Ketones by a Novel Technology: Dipolar Proton Transfer Reaction Mass Spectrometry (DP-PTR-MS), *Journal of the American Society for Mass Spectrometry*, 28, 873–879, <https://doi.org/10.1007/s13361-017-1638-7>, 2017.
- 860 Passananti, M., Zapadinsky, E., Zanca, T., Kangasluoma, J., Mylly, N., Rissanen, M. P., Kurtén, T., Ehn, M., Attoui, M., and Vehkamäki, H.: How well can we predict cluster fragmentation inside a mass spectrometer?, *Chemical Communications*, 55, 5946–5949, <https://doi.org/10.1039/C9CC02896J>, 2019.
- 865 Peterson, K. A., Figgen, D., Goll, E., Stoll, H., and Dolg, M.: Systematically convergent basis sets with relativistic pseudopotentials. II. Small-core pseudopotentials and correlation consistent basis sets for the post-*d* group 16–18 elements, *The Journal of Chemical Physics*, 119, 11 113–11 123, <https://doi.org/10.1063/1.1622924>, 2003.
- Riplinger, C. and Neese, F.: An efficient and near linear scaling pair natural orbital based local coupled cluster method, *The Journal of Chemical Physics*, 138, 034 106, <https://doi.org/10.1063/1.4773581>, 2013.
- 870 Riplinger, C., Sandhoefer, B., Hansen, A., and Neese, F.: Natural triple excitations in local coupled cluster calculations with pair natural orbitals, *The Journal of Chemical Physics*, 139, 134 101, <https://doi.org/10.1063/1.4821834>, 2013.
- Rissanen, M. P., Mikkilä, J., Iyer, S., and Hakala, J.: Multi-scheme chemical ionization inlet (MION) for fast switching of reagent ion chemistry in atmospheric pressure chemical ionization mass spectrometry (CIMS) applications, *Atmospheric Measurement Techniques*, 12, 6635–6646, <https://doi.org/10.5194/amt-12-6635-2019>, 2019.



- 875 Saiz-Lopez, A., Fernandez, R. P., Ordóñez, C., Kinnison, D. E., Gómez Martín, J. C., Lamarque, J.-F., and Tilmes, S.: Iodine chemistry in the troposphere and its effect on ozone, *Atmospheric Chemistry and Physics*, 14, 13 119–13 143, <https://doi.org/10.5194/acp-14-13119-2014>, 2014.
- Sanchez, J., Tanner, D. J., Chen, D., Huey, L. G., and Ng, N. L.: A new technique for the direct detection of HO₂ radicals using bromide chemical ionization mass spectrometry (Br-CIMS): initial characterization, *Atmospheric Measurement Techniques*, 9, 3851–3861, <https://doi.org/10.5194/amt-9-3851-2016>, 2016.
- 880 Saunders, S. M., Jenkin, M. E., Derwent, R. G., and Pilling, M. J.: Protocol for the development of the Master Chemical Mechanism, MCM v3 (Part A): tropospheric degradation of non-aromatic volatile organic compounds, *Atmospheric Chemistry and Physics*, 3, 161–180, <https://doi.org/10.5194/acp-3-161-2003>, 2003.
- Shen, J. and He, X.-C.: MARFORCE-Flowtube model, <https://github.com/momo-catcat/MARFORCE-flowtube>, 2023.
- 885 Sherwen, T., Evans, M. J., Carpenter, L. J., Andrews, S. J., Lidster, R. T., Dix, B., Koenig, T. K., Sinreich, R., Ortega, I., Volkamer, R., Saiz-Lopez, A., Prados-Roman, C., Mahajan, A. S., and Ordóñez, C.: Iodine’s impact on tropospheric oxidants: a global model study in GEOS-Chem, *Atmospheric Chemistry and Physics*, 16, 1161–1186, <https://doi.org/10.5194/acp-16-1161-2016>, 2016.
- Sipilä, M., Sarnela, N., Jokinen, T., Henschel, H., Junninen, H., Kontkanen, J., Richters, S., Kangasluoma, J., Franchin, A., Peräkylä, O., Rissanen, M. P., Ehn, M., Vehkamäki, H., Kurten, T., Berndt, T., Petäjä, T., Worsnop, D., Ceburnis, D., Kerminen, V.-M., Kulmala, M., and O’Dowd, C.: Molecular-scale evidence of aerosol particle formation via sequential addition of HIO₃, *Nature*, 537, 532–534, <https://doi.org/10.1038/nature19314>, 2016.
- 890 Smith, D. and Španěl, P.: Selected ion flow tube mass spectrometry (SIFT-MS) for on-line trace gas analysis, *Mass Spectrometry Reviews*, 24, 661–700, <https://doi.org/10.1002/mas.20033>, 2005.
- Tham, Y. J., He, X.-C., Li, Q., Cuevas, C. A., Shen, J., Kalliokoski, J., Yan, C., Iyer, S., Lehmusjärvi, T., Jang, S., Thakur, R. C., Beck, L., Kempainen, D., Olin, M., Sarnela, N., Mikkilä, J., Hakala, J., Marbouti, M., Yao, L., Li, H., Huang, W., Wang, Y., Wimmer, D., Zha, Q., Virkanen, J., Spain, T. G., O’Doherty, S., Jokinen, T., Bianchi, F., Petäjä, T., Worsnop, D. R., Mauldin, R. L., Ovadnevaite, J., Ceburnis, D., Maier, N. M., Kulmala, M., O’Dowd, C., Dal Maso, M., Saiz-Lopez, A., and Sipilä, M.: Direct field evidence of autocatalytic iodine release from atmospheric aerosol, *Proceedings of the National Academy of Sciences*, 118, e2009951 118, <https://doi.org/10.1073/pnas.2009951118>, 2021.
- 900 Thornton, J. A., Kercher, J. P., Riedel, T. P., Wagner, N. L., Cozic, J., Holloway, J. S., Dubé, W. P., Wolfe, G. M., Quinn, P. K., Middlebrook, A. M., Alexander, B., and Brown, S. S.: A large atomic chlorine source inferred from mid-continental reactive nitrogen chemistry, *Nature*, 464, 271–274, <https://doi.org/10.1038/nature08905>, 2010.
- Veres, P., Roberts, J. M., Warneke, C., Welsh-Bon, D., Zahniser, M., Herndon, S., Fall, R., and de Gouw, J.: Development of negative-ion proton-transfer chemical-ionization mass spectrometry (NI-PT-CIMS) for the measurement of gas-phase organic acids in the atmosphere, *International Journal of Mass Spectrometry*, 274, 48–55, <https://doi.org/10.1016/j.ijms.2008.04.032>, 2008.
- 905 Wang, M., He, X.-C., Finkenzeller, H., Iyer, S., Chen, D., Shen, J., Simon, M., Hofbauer, V., Kirkby, J., Curtius, J., Maier, N., Kurtén, T., Worsnop, D. R., Kulmala, M., Rissanen, M., Volkamer, R., Tham, Y. J., Donahue, N. M., and Sipilä, M.: Measurement of iodine species and sulfuric acid using bromide chemical ionization mass spectrometers, *Atmospheric Measurement Techniques*, 14, 4187–4202, <https://doi.org/10.5194/amt-14-4187-2021>, 2021a.
- 910 Wang, S., McNamara, S. M., Moore, C. W., Obrist, D., Steffen, A., Shepson, P. B., Staebler, R. M., Raso, A. R. W., and Pratt, K. A.: Direct detection of atmospheric atomic bromine leading to mercury and ozone depletion, *Proceedings of the National Academy of Sciences*, 116, 14 479–14 484, <https://doi.org/10.1073/pnas.1900613116>, 2019.



- Wang, X., Jacob, D. J., Downs, W., Zhai, S., Zhu, L., Shah, V., Holmes, C. D., Sherwen, T., Alexander, B., Evans, M. J., Eastham, S. D., Neuman, J. A., Veres, P. R., Koenig, T. K., Volkamer, R., Huey, L. G., Bannan, T. J., Percival, C. J., Lee, B. H., and Thornton, J. A.:
915 Global tropospheric halogen (Cl, Br, I) chemistry and its impact on oxidants, *Atmospheric Chemistry and Physics*, 21, 13 973–13 996,
<https://doi.org/10.5194/acp-21-13973-2021>, 2021b.
- Weigend, F. and Ahlrichs, R.: Balanced basis sets of split valence, triple zeta valence and quadruple zeta valence quality for H to Rn: Design and assessment of accuracy, *Physical Chemistry Chemical Physics*, 7, 3297, <https://doi.org/10.1039/b508541a>, 2005.
- Westmore, J. B. and Alauddin, M. M.: Ammonia chemical ionization mass spectrometry, *Mass Spectrometry Reviews*, 5, 381–465,
920 <https://doi.org/10.1002/mas.1280050403>, 1986.
- Wine, P. H., Thompson, R. J., Ravishankara, A. R., Semmes, D. H., Gump, C. A., Torabi, A., and Nicovich, J. M.: Kinetics of the reaction
 $\text{OH} + \text{SO}_2 + \text{M} \rightarrow \text{HOSO}_2 + \text{M}$. Temperature and pressure dependence in the fall-off region, *The Journal of Physical Chemistry*, 88,
2095–2104, <https://doi.org/10.1021/j150654a031>, 1984.
- Woodward-Massey, R., Taha, Y. M., Moussa, S. G., and Osthoff, H. D.: Comparison of negative-ion proton-transfer with iodide ion
925 chemical ionization mass spectrometry for quantification of isocyanic acid in ambient air, *Atmospheric Environment*, 98, 693–703,
<https://doi.org/10.1016/j.atmosenv.2014.09.014>, 2014.
- Zellner, R., Ewig, F., Paschke, R., and Wagner, G.: Pressure and temperature dependence of the gas-phase recombination of hydroxyl radicals,
The Journal of Physical Chemistry, 92, 4184–4190, <https://doi.org/10.1021/j100325a038>, 1988.
- Zhang, R., Xie, H.-B., Ma, F., Chen, J., Iyer, S., Simon, M., Heinritzi, M., Shen, J., Tham, Y. J., Kurtén, T., Worsnop, D. R., Kirkby, J.,
930 Curtius, J., Sipilä, M., Kulmala, M., and He, X.-C.: Critical Role of Iodous Acid in Neutral Iodine Oxoacid Nucleation, *Environmental
Science & Technology*, 56, 14 166–14 177, <https://doi.org/10.1021/acs.est.2c04328>, 2022.